geosciences

MDPI

Article

Paleoenvironment and Organic Matter Accumulation Mechanism of Shallow to Semi-Deep Lacustrine Shale: A Case Study of Member I of the Qingshankou Formation in the Changling Sag, Southern Songliao Basin

Leqi Liu [1], Hongxia Li [1,*], Bo Liu [1], Xi'ao Wang [1], Zhou Jiang [1], Boyang Wang [1], Jianguo Yang [2], Fei Xiao [2], Lijuan Cheng [1] and Yuhui Feng [3]

[1] State Key Laboratory of Continental Shale Oil, Northeast Petroleum University, Daqing 163318, China; liubo@nepu.edu.cn (B.L.); chenglijuan@nepu.edu.cn (L.C.)
[2] Shenyang Center of China Geological Survey (Northeast Geological Science and Technology Innovation Center), Shenyang 110034, China
[3] College of Paleontology, Shenyang Normal University, Shenyang 110034, China
* Correspondence: lihx@nepu.edu.cn

Abstract

The Member I of the Qingshankou Formation (91.89~90.97 Ma) is the most significant lacustrine shale in the Songliao Basin, and preserves a continuous and complete record of terrestrial paleoenvironmental conditions and organic matter (OM) accumulation during the early Late Cretaceous. Although its abundant OM has traditionally been attributed to deep-lake anoxia, the accumulation mechanism in shallow to semi-deep lake settings remains unclear. To address this gap, samples from the JYY1 well in the Changling Sag were analyzed for TOC, iron species, and major/trace elements. The Al_2O_3/TiO_2 ratios and PAAS-normalized REEs patterns indicate the provenance is predominantly felsic to intermediate rocks, broadly compatible with tonalite. Geochemical proxies (τNa, V/Cr, Fe_{HR}/Fe_T, Fe_{py}/Fe_{HR}, B/Ga, Ti/Al, etc.) indicate a relatively humid climate, ferruginous to ferruginous-euxinic bottom waters, and brackish to saline conditions during the Member I deposition. In shallow to semi-deep lacustrine settings, redox conditions and detrital dilution were the principal controls on OM accumulation. The upper interval exhibits higher TOC because of improved OM preservation under ferruginous-euxinic bottom-water and weaker detrital dilution. In contrast, stronger detrital dilution and ferruginous bottom waters contributed to the lower TOC of the lower interval. These findings suggest that widespread pyrite occurrence and elevated Fe_{py}/Fe_{HR} ratios may help identify organic-rich shale intervals and guide shale oil and gas exploration.

Keywords: paleoenvironment; organic matter accumulation; elemental geochemistry; shallow lake; the Member I Changling Sag

Check for updates

Academic Editor: Massimo Zecchin

Received: 10 September 2026
Revised: 21 October 2026
Accepted: 26 October 2026
Published: 1 November 2026

Copyright: © 2026 by the authors. Licensee MDPI, Basel, Switzerland. This article is an open access article distributed under the terms and conditions of the Creative Commons Attribution (CC BY) license.

1. Introduction

Black shale plays an important role in hydrocarbon generation and also provides reservoir space for shale oil and gas accumulation [1]. It preserves critical records of climatic and environmental conditions during deposition, making it valuable for studying greenhouse climates, atmospheric O_2 and CO_2 fluctuations, anoxic events (in both lacustrine and marine settings), biotic evolution, and continental weathering [2,3]. During the Late Cretaceous

(91.89–90.97 Ma), the Songliao Basin experienced a pronounced lake transgression associated with the deposition of Member I of the Qingshankou Formation, which promoted extensive black shale deposition. Member I represents an important interval of hydrocarbon source rocks with considerable potential for shale oil exploration in the Songliao Basin [4,5]. The vertical continuity, extensive distribution, and high organic carbon content of Member I shale make it suitable for investigating paleoenvironmental changes and the processes responsible for organic matter enrichment.

Organic matter enrichment in shales reflects the combined influence of organic production, settling, preservation, and burial processes [6,7]. Their relative contributions depend on paleoenvironmental conditions, including paleoclimate, lake depth, redox state, paleosalinity, terrigenous detrital input, and paleoproductivity [8]. Paleoproductivity is essential for organic matter formation. Oxygen-depleted bottom waters promote organic matter preservation by suppressing oxidative degradation. Terrigenous detrital input delivers nutrients to the lake system and may also play a role in dilution during organic matter burial [9–11]. Therefore, the factors governing organic matter enrichment vary markedly among different sedimentary basins. Changes in lake level (or sea level) may alter hydrodynamic energy, detrital supply, and the redox state of bottom waters, thereby changing which processes primarily control organic matter accumulation at different depositional stages [12].

Previous research on shale paleoenvironment and organic matter enrichment has mainly addressed marine and deep-lake deposits, with comparatively limited investigation of shallow to semi-deep lacustrine environments, especially slope areas experiencing rapid hydrological changes. The Changling Sag, situated in the southern part of the Songliao Basin, is characterized by multiple-circular slope breaks that influenced the distribution of deltaic, shallow lacustrine, and semi-deep to deep lacustrine facies during the Member I deposition [13]. Such a depositional setting allows paleoenvironmental changes in shallow to semi-deep lacustrine shales to be examined alongside their organic matter enrichment mechanisms. Studies on the paleoenvironment and the processes governing organic matter accumulation of the Member I in the Changling Sag have achieved many findings. Using continuous elemental profiles obtained from lithology-scanning logs, Bai et al. investigated the relationship between paleoenvironmental conditions and residual hydrocarbons, identifying paleoclimate and redox conditions as important controls on residual hydrocarbon enrichment [14]. Based on major-element and trace-element compositions and biomarkers, Ma et al. and Meng et al. linked differences in organic matter enrichment to variations in its sources and the lake's salinity [15,16]. From TOC and major-element and trace-element data, Cheng et al. distinguished three organic matter accumulation models corresponding to different lake environments: productivity-dominated model in shallow lakes, combined productivity and preservation control in semi-deep lakes, and preservation-dominated model in deep lakes [9]. Using organic petrological observations and framboidal pyrite size distributions, researchers have highlighted the contribution of clay minerals to the preservation of terrigenous organic matter [17]. However, interpretations of organic matter enrichment models remain inconsistent. Such discrepancies may reflect variations in well locations and sampling intervals, differences in paleoenvironmental proxy thresholds, interactions among multiple controlling factors, and variations in the resolution and sensitivity of analytical methods.

This study focuses on the shale succession of the Member I recovered from the JYY1 well in the Changling Sag. Iron speciation, major-element, trace-element, and rare earth-element data are integrated to reconstruct the depositional environment. Based on iron species, we can further identify redox conditions such as ferruginous, ferruginous-euxinic, and euxinic, which have not been discussed in the study area. By integrating these geochemical

results with total organic carbon (TOC), this study identifies the principal factors governing organic matter accumulation and explores how paleoenvironmental evolution influenced organic matter accumulation in shallow to semi-deep lacustrine settings.

2. Geological Backgrounds

Situated in northeastern China, the Songliao Basin constitutes an important continental petroliferous basin extending mainly along a northeast–southwest axis [18]. The basin is subdivided into six first-order tectonic units: the Central Depression, Northern Plunge, Western Slope, Southwestern Uplift, Northeastern Uplift, and Southeastern Uplift [19]. The Central Depression contains the Qijia-Gulong and Sanzhao Sags in its northern part and the Changling Sag in its southern part (Figure 1a; [19]). The Changling Sag exhibits lower elevations in its eastern part than the western part, while its southern slopes are steeper than those in the north [14,16].

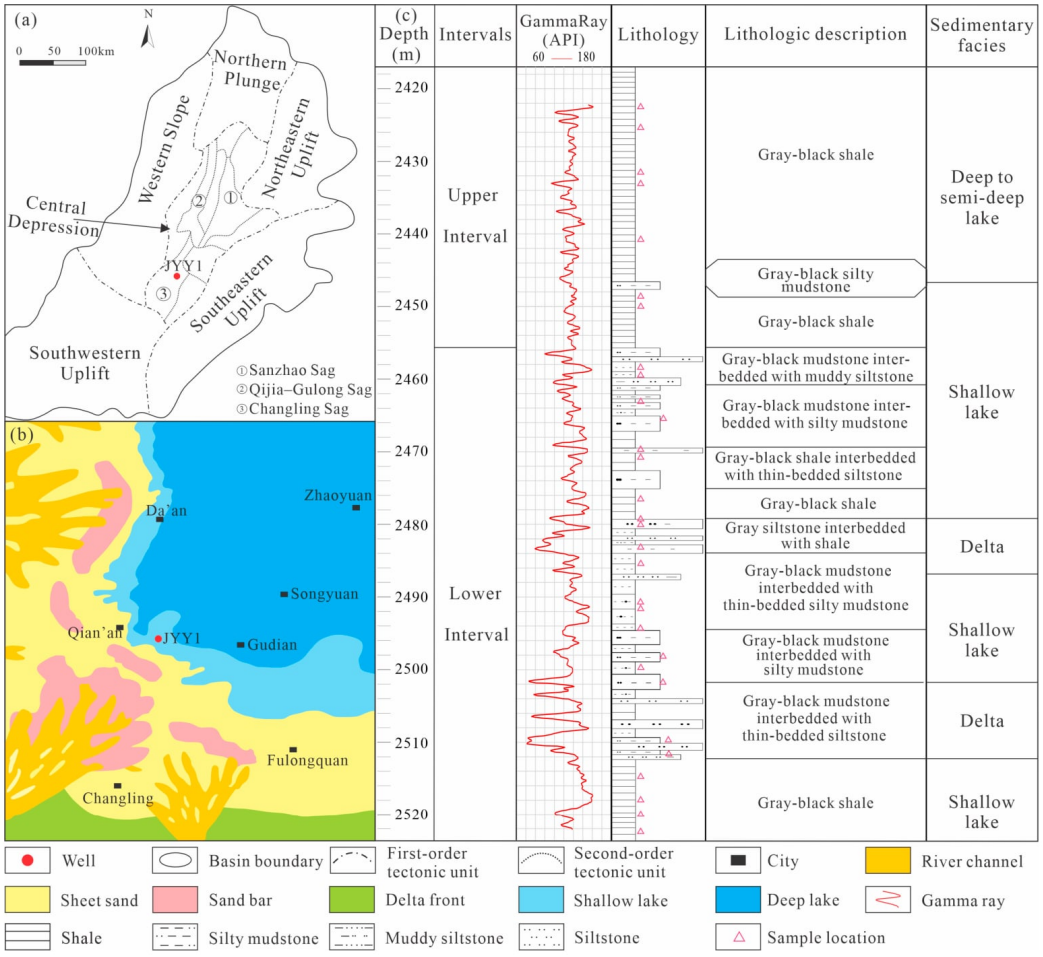


Figure 1. (**a**) The first-order and second-order structural units of the Songliao Basin. (**b**) Sedimentary facies of the Member I across the Changling Sag [13]. The red solid circle indicates the location of the JYY1 well. (**c**) Lithological column of the Member I of the JYY1 well [16].

During the deposition of the Member I (91.89~90.97 Ma), the Changling Sag underwent its maximum lake transgression, leading to the formation of dark gray to black shale and silty mudstones with considerable hydrocarbon generation potential [20,21]. The paleogeomorphology of the Changling Sag is characterized by multiple stepped slope breaks, which can be broadly divided into gentle slope and deep depressional zones [13,22]. The JYY1 well, located at the transitional zone separating the gentle slope from the deep depressional zone [22], occurs at the boundary between deltaic and lacustrine depositional

systems (Figure 1b; [14,23]). The lower interval of the Member I develops both shallow to semi-deep lacustrine and deltaic facies, with lithologies dominated by dark gray shale intercalated with thin siltstone and argillaceous siltstone beds. In contrast, the upper interval is predominantly characterized by deep to semi-deep lacustrine dark gray to black shales with minor thin interbeds of argillaceous siltstone (Figure 1c; [14,23]).

3. Samples and Methods

Thirty core samples were obtained from the JYY1 well over the depth interval of 2422.4~2522.1 m, with sampling intervals of 0.5~8.3 m (average of 3.4 m). To reduce potential grain-size effects on paleoenvironmental interpretations, sampling was restricted to shale, silty mudstone, and a small number of muddy siltstone, while siltstone was excluded (Figure 2). The sampling density and stratigraphic coverage are considered adequate to indicate the paleoenvironmental evolution of the Member I. All 30 samples were crushed to a particle size of >200 meshes (i.e., <75 μm) prior to subsequent analyses, including major and trace elements. For closely spaced samples showing similar lithological and paleoenvironmental characteristics, one representative sample was selected for TOC and iron speciation analyses. Consequently, these measurements were performed on 16 samples.



Figure 2. Photographs of the collected samples in the Member I. (**a**) JYY1-3, 2422.38 m, black shale. (**b**) JYY1-32, 2431.48 m, black shale. (**c**) JYY1-7, 2440.50 m, black shale. (**d**) JYY1-13, 2479.9 m, gray muddy siltstone with wavy beddings. (**e**) JYY1-23, 2497.50 m, black-gray silty mudstone. (**f**) JYY1-9, 2458.25 m, black-gray muddy siltstone with horizontal beddings.

3.1. TOC and Rock-Eval Pyrolysis

To determine total organic carbon (TOC), inorganic carbon was eliminated by treating the samples with an HCl–H_2O mixture (1:7) at 60–80 °C for 2 h. Following acid treatment, the residues were repeatedly rinsed with deionized water to eliminate the remaining acid

and subsequently dried at 60 °C. TOC concentrations were measured with a LECO CS-230 carbon–sulfur analyzer. The analysis followed the Chinese national standard GB/T 19145–2022 [24]. Untreated sample aliquots were analyzed by Rock-Eval pyrolysis with a Rock-Eval 6 instrument to obtain T_{max}, S_1, S_2, and S_3. The hydrogen index (HI) was calculated as HI = (S_2/TOC) × 100 (mg/g).

3.2. Iron Species

Sequential extraction of highly reactive iron (Fe_{HR}) species was performed according to Poulton and Canfield [25]. Pyrite-host iron (Fe_{py}) was initially isolated via the chromium-reduction technique [26]. The carbonate-associated iron (Fe_{carb}), oxidizable iron (Fe_{ox}), and magnetite-bound iron (Fe_{mag}) were recovered through stepwise chemical treatments as specified in the original protocol. The total Fe_{HR} concentration was calculated as the sum of the four operational fractions. All extraction procedures were carried out at the Chengdu University of Technology.

3.3. Major Elements

The powdered samples were dried and weighed, and their initial mass was recorded as W1. The samples were subsequently calcined at 1000 °C for 2 h, and the remaining mass was measured as W2. The Loss on ignition (LOI) was calculated using Equation (1):

$$LOI = [(W1 - W2)/W1] \times 100\%. \quad (1)$$

Following ignition, the ashed material was fused with a flux mixture ($Li_2B_4O_{72}$-$LiBO_2$-LiF = 9:2:1), using NH_4NO_3 as the oxidizing agent. Ten major oxides, including SiO_2, Al_2O_3, Na_2O, K_2O, MgO, CaO, Fe_2O_3, MnO, TiO_2, and P_2O_5, were quantified using an Axios PW4400/40 X-ray fluorescence spectrometer made by the PANalytical (Almelo, the Netherlands), with results expressed in wt.%. The measurements were conducted following the Chinese national standard GB/T 14506.28–2010 [27].

3.4. Trace Elements (Including Rare Earth Elements)

For trace-element (Sc, V, Cr, Co, Ni, Cu, Zn, Zr, Th, U, Rb, Sr, Ba, Mo, Cd) and rare earth element (REE; La, Ce, Pr, Nd, Sm, Eu, Gd, Tb, Dy, Y, Ho, Er, Tm, Yb, Lu) analyses, 50 mg portions of powdered samples were digested in sealed vessels with HCl–HF–HNO_3 at 200 °C for 48 h. After cooling and drying, the remaining sample was mixed with 2 mL of 30% HNO_3 and maintained at 140 °C for 12 h. The resulting solutions were diluted to the required volume with 1% HNO_3 and subsequently analyzed using inductively coupled plasma mass spectrometry (ICP-MS). An internal Rh standard was added to monitor instrumental signal stability, and a procedural blank was processed in parallel to correct for background interference and possible contamination, as recommended by Carvalho et al. [28]. Relative standard deviations (%RSD) were below 5% for all analyzed elements.

4. Results

4.1. TOC and Rock-Eval Pyrolysis Parameters

TOC is commonly employed as an indicator of organic matter abundance in source rock assessment. TOC values in the Member I range from 0.32% to 2.87%, averaging 1.30% (Table 1). In the lower interval, TOC varies between 0.32% and 2.86%, with a mean of 1.00%. By comparison, the upper interval has TOC values of 1.64–2.87%, averaging 2.20%. Thus, the upper interval is characterized by greater organic matter abundance than the lower interval. T_{max} values are 439–457 °C (mean: 446 °C) in the lower interval and 440–450 °C (mean: 445 °C) in the upper interval, suggesting that both intervals are thermally mature.

Given their comparable maturity levels, depositional conditions may have played a more important role in the observed differences in TOC.

Table 1. Total organic carbon (TOC) contents and Rock-Eval pyrolysis results for Member I samples from the JYY1 well.

Interval	Sample No.	Depth (m)	HI (mg/g)	T_{max} (°C)	S_1 (mg/g)	S_2 (mg/g)	$S_1 + S_2$ (mg/g)	TOC (%)
Upper interval	JYY1-3	2422.4	362.92	440	1.32	5.95	7.27	1.64
	JYY1-32	2431.5	353.54	447	1.65	10.13	11.78	2.87
	JYY1-7	2440.5	368.04	443	1.22	6.21	7.43	1.69
	JYY1-6	2448.6	450.95	450	1.35	11.68	13.03	2.59
	Average		383.86	445	1.39	8.49	9.88	8.49
Lower interval	JYY1-9	2458.3	236.37	439	0.21	0.98	1.19	0.41
	JYY1-25	2465.5	363.59	444	0.98	4.29	5.27	1.18
	JYY1-11	2469.6	449.37	451	1.34	12.83	14.17	2.86
	JYY1-14	2470.6	377.60	445	1.16	5.69	6.85	1.51
	JYY1-13	2479.9	202.09	447	0.32	1.04	1.36	0.51
	JYY1-16	2485.5	208.04	440	0.32	1.09	1.41	0.52
	JYY1-22	2491.5	313.77	441	0.82	4.72	5.54	1.50
	JYY1-20	2494.2	171.01	453	0.21	0.6	0.81	0.35
	JYY1-17	2499.8	277.53	444	0.58	2.6	3.18	1.14
	JYY1-26	2511.8	227.51	457	0.26	0.73	0.99	0.32
	JYY1-28	2518	197.40	451	0.36	1.34	1.70	0.68
	JYY1-30	2522.1	200.49	443	0.38	2.03	2.41	1.01
	Average		264.56	446	0.58	3.16	3.74	3.16

The upper and lower intervals have mean HI values of 383.86 and 264.56 mg/g, respectively, and corresponding mean T_{max} values of 445.0 and 446.25 °C (Table 1). In the HI–T_{max} diagram, most samples from the upper interval occupy the type II_1 kerogen field, whereas a few are located within the type I field (Figure 3a). Samples from the lower interval are predominantly distributed in the type II_1 field, with several plotting near the type II_2 field. Both intervals exhibit similar levels of thermal maturity (Figure 3a). According to the TOC–($S_1 + S_2$) diagram, most upper-interval samples correspond to good source rocks, with an average $S_1 + S_2$ of 9.88 mg/g (Figure 3b). Conversely, the lower-interval samples fall within poor to good source rock categories, with an average of 3.74 mg/g (Figure 3b). These results indicate higher organic matter abundance and hydrocarbon generation potential in the upper interval.

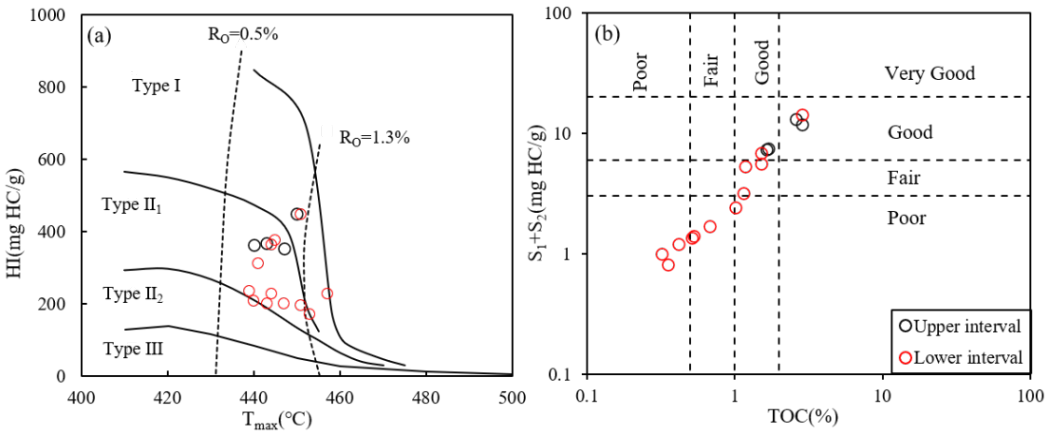


Figure 3. Assessment of source rock characteristics based on (**a**) the HI–T_{max} relationship and (**b**) the TOC–($S_1 + S_2$) relationship. The criteria used in both plots are adopted from the Chinese industry specification SY/T 5735–2019 [29].

4.2. Iron Species

The formation of pyrite through reactions between highly reactive iron (Fe_{HR}) and H_2S under anoxic conditions provides the basis for using Fe_{py}/Fe_{HR} and Fe_{HR}/Fe_T ratios to assess depositional redox conditions [25,30]. Previous studies have proposed Fe_{HR}/Fe_T thresholds of 0.22 and 0.38 for distinguishing oxic, potentially anoxic, and anoxic conditions. Under anoxic conditions, Fe_{py}/Fe_{HR} values below 0.7 are generally associated with ferruginous settings, whereas values above 0.8 suggest euxinic conditions [31,32]. In the JYY1 well, Fe_{HR}/Fe_T values for Member I range from 0.30 to 0.55, consistent with potentially anoxic to anoxic conditions. The Fe_{py}/Fe_{HR} ratios vary between 0.02 and 0.58, with all values below 0.7, supporting ferruginous conditions (Table 2).

Table 2. Total iron (Fe_T) and iron speciation compositions for the Member I in JYY1 well.

Interval	Sample No.	Depth (m)	Fe_T (%)	Fe_{py} (%)	Fe_{carb} (%)	Fe_{ox} (%)	Fe_{mag} (%)	Fe_{HR} (%)	Fe_{HR}/Fe_T	Fe_{py}/Fe_{HR}
Upper interval	JYY1-3	2422.4	3.87	1.05	0.42	0.17	0.17	1.81	0.47	0.58
	JYY1-32	2431.5	3.61	0.85	0.46	0.15	0.16	1.62	0.45	0.52
	JYY1-7	2440.5	3.41	0.60	0.73	0.15	0.13	1.61	0.47	0.37
	JYY1-6	2448.6	3.59	0.78	0.46	0.08	0.14	1.46	0.41	0.53
	Average		3.62	0.82	0.52	0.14	0.15	1.63	0.45	0.50
Lower interval	JYY1-9	2458.3	3.15	0.56	0.55	0.13	0.20	1.44	0.46	0.39
	JYY1-25	2465.5	4.50	0.94	0.59	0.12	0.34	1.99	0.44	0.47
	JYY1-11	2469.6	4.11	0.33	0.61	0.11	0.38	1.42	0.35	0.23
	JYY1-14	2470.6	4.86	0.45	0.72	0.15	0.51	1.83	0.38	0.25
	JYY1-13	2479.9	3.16	0.14	0.45	0.14	0.20	0.94	0.30	0.14
	JYY1-16	2485.5	3.41	0.11	0.82	0.14	0.26	1.33	0.39	0.08
	JYY1-22	2491.5	4.37	0.80	0.66	0.18	0.3	2.00	0.46	0.40
	JYY1-20	2494.2	4.18	0.08	0.88	0.22	0.2	1.47	0.35	0.05
	JYY1-17	2499.8	4.36	0.70	0.52	0.16	0.26	1.64	0.38	0.43
	JYY1-26	2511.8	3.76	0.02	0.75	0.15	0.28	1.21	0.32	0.02
	JYY1-28	2518	3.70	0.31	0.34	0.14	0.31	1.11	0.30	0.28
	JYY1-30	2522.1	3.93	1.17	0.57	0.20	0.22	2.17	0.55	0.54
	Average		3.96	0.47	0.62	0.15	0.30	1.55	0.39	0.27

4.3. Major and Trace Elements

The geochemical characteristics of major and trace elements serve as important proxies for constraining sediment provenance and depositional environments. The Member I shale is dominated by SiO_2 (52.0~65.4%) and Al_2O_3 (12.7~20.2%). Specifically, the upper interval exhibits average SiO_2 and Al_2O_3 contents of 57.6% and 17.9%, respectively, whereas the lower interval shows values of 58.9% and 16.6%, respectively. This vertical variation is consistent with the lithological transition from mudstone-dominated facies in the upper interval to increased silty intercalations in the lower interval. The concentrations of Fe_2O_3, K_2O, Na_2O, MgO, and CaO are all below 8%, while those of TiO_2, P_2O_5, and MnO are each less than 1% (Table 3). Notably, the relatively low CaO (<7.1%) and MgO (<3.0%) contents suggest that calcite and dolomite are not abundantly developed in the Member I shale.

In this study, trace element abundances in the Member I samples (Table 4) were expressed relative to the Upper Continental Crust (UCC) and presented as spider diagrams (Figure 4). The resulting patterns reveal marked differences in elemental enrichment. Among the terrigenous elements, Zr and Th exhibit UCC-normalized values of approximately 2, indicating obvious enrichment. In contrast, Sc has a mean normalized value of 1.3, close to the UCC, although slight enrichment occurs in a few samples. Redox-sensitive elements, including Mo, V, Ni, and U, show varying degrees of enrichment. Mo exhibits the highest abundance, at 5.1 × UCC, followed by Ni (average 3.2), while V and

U show moderate enrichment, with averages of 2.6 and 1.9 times of the UCC, respectively. Productivity-related elements Cu and Zn exhibit weak to moderate enrichment, with average values of 1.8 and 1.6 times of the UCC, respectively. In contrast, Ba and Sr, which are commonly used as indicators for paleosalinity, are generally close to the UCC or exhibit slight depletion, with normalized averages of 0.7 and 0.9 times of the UCC, respectively.

Table 3. Major elemental content for the JYY1 well in Member I.

Interval	Sample No.	Depth (m)	SiO_2 (%)	Al_2O_3 (%)	Fe_2O_3 (%)	CaO (%)	MgO (%)	K_2O (%)	Na_2O (%)	TiO_2 (%)	P_2O_5 (%)	MnO (%)	LOI (%)
Upper interval	JYY1-3	2422.4	57.5	19.1	5.5	1.0	2.0	4.5	2.0	0.67	0.27	0.06	7.08
	JYY1-4	2425.4	57.0	17.9	6.0	2.1	2.0	4.1	2.1	0.62	0.17	0.08	7.49
	JYY1-32	2431.5	58.3	18.2	5.2	0.9	1.8	3.6	2.6	0.67	0.18	0.05	8.15
	JYY1-5	2433	57.7	17.6	6.2	1.1	2.1	3.6	2.6	0.69	0.13	0.08	8.14
	JYY1-7	2440.5	53.8	17.3	4.9	3.8	2.9	3.9	2.2	0.67	0.17	0.09	10.02
	JYY1-6	2448.6	58.0	18.0	5.1	1.9	1.8	4.0	2.5	0.66	0.15	0.04	7.71
	JYY1-8	2450	60.5	17.2	4.8	2.3	1.7	4.0	2.4	0.64	0.13	0.07	5.79
	Average		57.6	17.9	5.4	1.9	2.1	4.0	2.3	0.66	0.17	0.07	7.77
Lower interval	JYY1-9	2458.3	64.1	15.8	4.5	1.7	1.5	3.8	2.7	0.65	0.22	0.07	4.54
	JYY1-10	2459.3	65.4	14.3	5.0	2.1	1.8	2.9	2.9	0.70	0.19	0.12	4.46
	JYY1-2	2463	62.6	12.7	4.5	5.4	1.4	2.8	2.6	0.53	0.13	0.16	6.89
	JYY1-25	2465.5	53.8	16.4	6.4	5.2	2.5	4.1	1.7	0.62	0.21	0.09	8.8
	JYY1-11	2469.6	55.2	17.1	5.9	2.9	2.2	4.0	2.4	0.63	0.15	0.09	9.26
	JYY1-14	2470.6	56.9	16.6	6.9	2.0	2.5	4.1	2.1	0.62	0.15	0.09	7.82
	JYY1-12	2476.4	57.9	16.8	6.6	1.7	2.2	4.1	2.3	0.68	0.17	0.10	7.47
	JYY1-15	2479.4	59.6	20.2	4.4	0.7	2.0	4.8	2.4	0.84	0.23	0.04	4.74
	JYY1-13	2479.9	63.9	16.6	4.5	1.4	1.6	3.8	2.8	0.68	0.20	0.08	4.01
	JYY1-18	2483.1	60.7	17.8	5.0	1.0	1.9	4.3	2.6	0.69	0.17	0.07	5.75
	JYY1-16	2485.5	60.4	16.5	4.9	2.5	2.0	4.1	2.5	0.66	0.18	0.09	6.17
	JYY1-19	2490.6	57.8	18.3	5.9	1.2	2.1	4.6	1.7	0.66	0.17	0.05	7.32
	JYY1-22	2491.5	55.9	16.9	6.2	3.1	2.6	4.2	1.8	0.66	0.21	0.10	8.19
	JYY1-20	2494.2	51.9	17.3	6.0	5.4	3.0	4.4	1.5	0.77	0.27	0.10	9.03
	JYY1-23	2497.5	62.6	15.2	5.9	2.5	2.0	3.4	2.4	0.71	0.22	0.08	4.96
	JYY1-17	2499.8	61.5	16.9	6.2	1.1	1.8	3.8	2.5	0.65	0.18	0.06	5.13
	JYY1-21	2501.8	57.8	17.4	5.6	1.6	2.5	4.4	2.0	0.69	0.18	0.08	7.43
	JYY1-31	2509.8	61.1	17.8	5.0	1.7	1.9	4.3	2.1	0.70	0.15	0.04	5.05
	JYY1-26	2511.8	57.3	16.3	5.4	4.6	2.0	4.0	1.8	0.71	0.15	0.09	7.51
	JYY1-27	2514.6	58.1	17.9	6.2	1.3	2.1	4.3	2.2	0.63	0.12	0.07	6.63
	JYY1-28	2518	58.7	16.1	5.3	3.9	2.4	3.	1.9	0.68	0.17	0.08	6.73
	JYY1-29	2520	53.8	14.8	5.9	7.1	2.8	3.5	1.5	0.69	0.21	0.14	9.13
	JYY1-30	2522.1	57.9	15.8	5.6	4.3	1.8	3.8	2.4	0.63	0.27	0.10	7.03
	Average		58.9	16.6	5.6	2.8	2.1	4.0	2.2	0.67	0.19	0.09	6.70

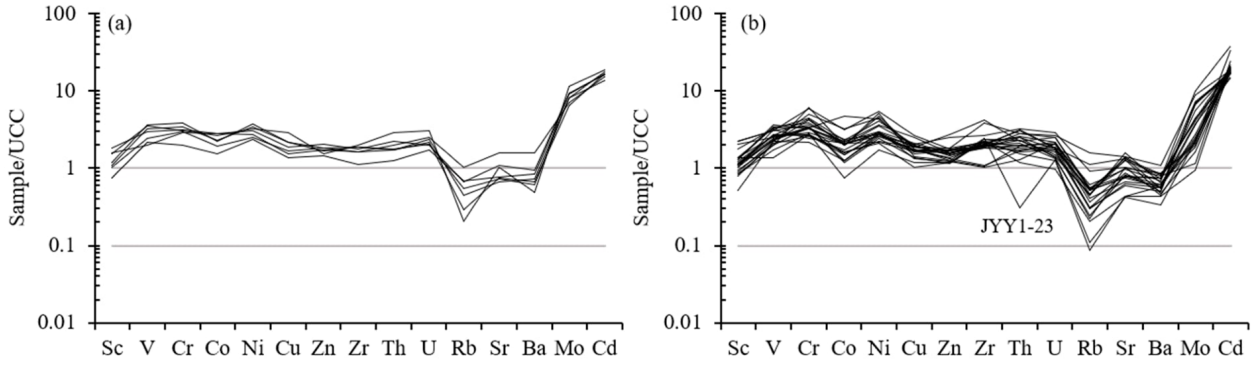


Figure 4. Spider diagram showing trace element concentrations of (**a**) the upper interval and (**b**) the lower interval for the Member I samples from the Changling Sag. Each black polyline corresponds to one sample measured in this study. Elemental abundances are expressed relative to the upper continental crust (UCC) reference values reported by Taylor and McLennan [33].

Table 4. Trace elemental compositions for the JYY1 well in Member I, all in μg/g content.

Interval	Sample No.	Depth (m)	Sc	V	Cr	Co	Ni	Cu	Zn	Zr	Th	U	Rb	Sr	Ba	Mo	Cd
Upper interval	JYY1-3	2422.4	11	144	103	19	51	42	128	310	18	6.6	50	237	397	12	1.3
	JYY1-4	2425.4	20	177	111	28	62	46	147	341	24	5.6	74	382	513	14	1.6
	JYY1-32	2431.5	13	218	134	22	75	54	119	360	19	5.8	61	254	337	12	1.7
	JYY1-5	2433	12	196	121	23	69	54	130	354	19	6.0	33	264	368	10	1.6
	JYY1-7	2440.5	17	212	108	27	64	73	108	374	31	8.7	23	357	266	17	1.8
	JYY1-6	2448.6	8	128	70	15	47	34	103	210	13	4.8	78	269	468	14	1.6
	JYY1-8	2450	17	121	100	28	55	38	123	307	22	7.0	115	555	868	11	1.5
	Average		14	171	107	23	60	49	123	322	21	6.4	62	331	460	13	1.6
Lower interval	JYY1-9	2458.3	9	118	122	12	49	35	81	418	13	2.7	23	151	318	4	2.0
	JYY1-10	2459.3	9	103	97	8	34	29	85	423	16	3.5	10	151	241	1	2.0
	JYY1-2	2463	15	81	94	16	42	25	84	447	24	4.2	50	555	358	3	2.0
	JYY1-25	2465.5	11	118	211	20	103	35	88	200	21	6.0	52	497	400	7	1.5
	JYY1-11	2469.6	10	132	76	13	55	43	96	208	18	5.8	68	344	381	11	1.7
	JYY1-14	2470.6	9	126	89	17	59	33	86	197	14	5.9	46	236	333	6	1.5
	JYY1-12	2476.4	25	182	128	24	55	49	118	356	30	7.5	175	487	600	13	1.8
	JYY1-15	2479.4	15	197	121	13	51	51	179	504	35	8.0	102	359	432	2	2.4
	JYY1-13	2479.9	12	139	177	32	90	40	129	730	30	7.0	60	348	471	3	3.3
	JYY1-18	2483.1	13	159	95	16	44	47	129	413	21	4.8	57	267	407	6	2.0
	JYY1-16	2485.5	13	144	119	15	57	40	121	401	27	6.1	61	435	450	6	1.8
	JYY1-19	2490.6	14	219	113	23	60	52	111	349	19	5.3	34	210	277	11	1.7
	JYY1-22	2491.5	20	196	153	23	82	49	107	345	21	5.7	41	300	272	10	1.7
	JYY1-20	2494.2	25	181	206	31	110	65	124	352	27	3.9	25	357	244	3	1.7
	JYY1-23	2497.5	6	133	146	20	95	44	90	468	3	3.6	12	149	185	3	2.2
	JYY1-17	2499.8	12	137	117	48	86	46	195	805	24	7.1	64	275	411	15	3.7
	JYY1-21	2501.8	14	208	133	22	73	63	112	363	20	4.6	35	275	311	8	1.8
	JYY1-31	2509.8	12	166	94	15	55	43	122	420	27	4.9	59	265	315	4	2.1
	JYY1-26	2511.8	23	148	117	21	52	43	97	376	33	5.1	127	463	456	3	2.0
	JYY1-27	2514.6	11	187	84	21	44	42	113	393	18	4.8	34	223	305	10	1.8
	JYY1-28	2518	15	153	101	20	55	38	120	380	23	3.8	28	283	338	4	1.8
	JYY1-29	2520	13	161	150	20	71	49	104	365	24	4.0	52	456	263	2	1.7
	JYY1-30	2522.1	11	140	112	21	58	46	110	388	33	5.0	58	481	303	5	2.0
	Average		14	153	124	20	64	44	113	404	23	5.2	55	329	351	6	2.0

5. Discussion

5.1. Provenance

Identifying the parent rocks is a prerequisite for reliable paleoenvironmental reconstruction, because variations in sediment provenance may affect sample composition and the interpretation of paleoenvironmental proxies. Aluminum (Al) and titanium (Ti) exhibit relatively limited mobility during sediment transport and deposition, and their ratios largely reflect the composition of the source rocks. Hayashi et al. [34] demonstrated that the Al_2O_3/TiO_2 ratio in fine-grained sedimentary rocks effectively preserves signatures of their parent rock, with Al_2O_3/TiO_2 ratios of 3~8 for mafic igneous rocks, 8~21 for intermediate igneous rocks, and 21~70 for felsic igneous rocks (Figure 5). As shown in Figure 5, the Member I samples from the JYY1 well predominantly plot within the felsic igneous zone, which is determined to be the parent rock. Furthermore, the potential parent rocks including gneiss, gabbro, tonalite, and granite are plotted in Figure 5, which shows that tonalite has the closest Al_2O_3/TiO_2 ratio to that of the studied samples.

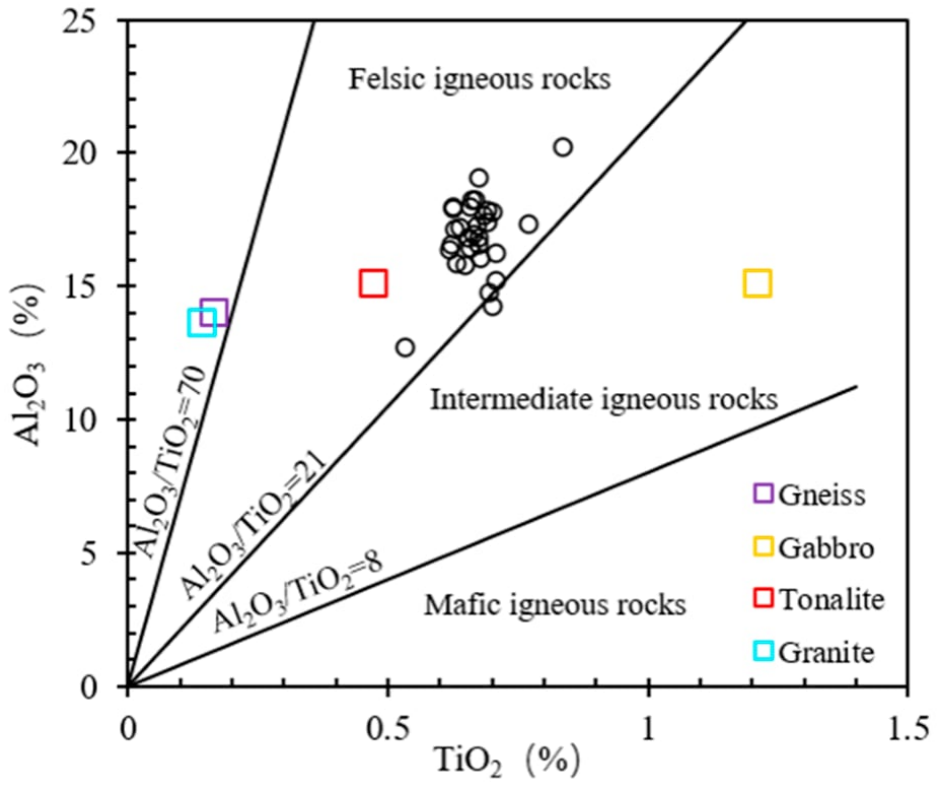


Figure 5. Plot of TiO_2 versus Al_2O_3 for the Member I in the JYY1 well. All the black circles are samples in this study. Dividing lines of Al_2O_3/TiO_2 are in accordance with Hayashi et al. [34]. The potential parent-rock data represent basement rocks of the Songliao Basin, whose lithological compositions are comparable to those exposed in the adjacent Zhangguangcai, Great Xing'an, and Lesser Xing'an Ranges [35].

Rare earth elements (REEs) are chemically stable and barely affected by weathering or diagenetic alteration, making them reliable tracers for provenance discrimination [36,37]. With the exception of sample JYY1-23, all other samples exhibit similar PAAS-normalized REEs distribution patterns, characterized by relatively flat trends (Figure 6), indicating the absence of significant fractionation between light REEs (LREEs) and heavy REEs (HREEs). This consistency points to a common source affinity. In contrast, the PAAS-normalized REEs patterns of gneiss, gabbro, and granite differ markedly from those of the Member I samples (Figure 6). Tonalite, however, exhibits a relatively flat PAAS-normalized REEs distribution pattern that closely resembles that of the Member I samples (Figure 6).

Unlike the other samples, JYY1-23 displays an REE distribution pattern inclined toward the left after the PAAS normalization, together with a low $(La/Yb)_N$ value of 0.1 (Table A1), reflecting relative HREE enrichment. This sample also yields a notably high Zr/Rb ratio of 38.4 (Table 5), reflecting an increased contribution of Zr-rich coarse-grained detrital components and a corresponding decrease in Rb-rich clay minerals, both of which point to intensified hydrodynamic conditions during deposition. Given that clay minerals and other fine-grained suspended particulates are the primary carriers of REEs [38], the clearly low REEs concentration of 49 in this sample is likely due to reduced input of fine-grained clay fractions. Furthermore, grain-size sorting may have modified the relative proportions of different REEs-bearing minerals, thereby leading to relative depletion of LREEs. In addition, plagioclase typically exhibits positive Eu anomalies [33], and the weak positive Eu anomaly of 1.11 observed in this sample (Table A1) further suggests an increased contribution of feldspar-rich components. Collectively, these geochemical anomalies in sample JYY1-23 can

be primarily attributed to an increased influx of silty fractions in response to transiently enhanced hydrodynamic conditions.

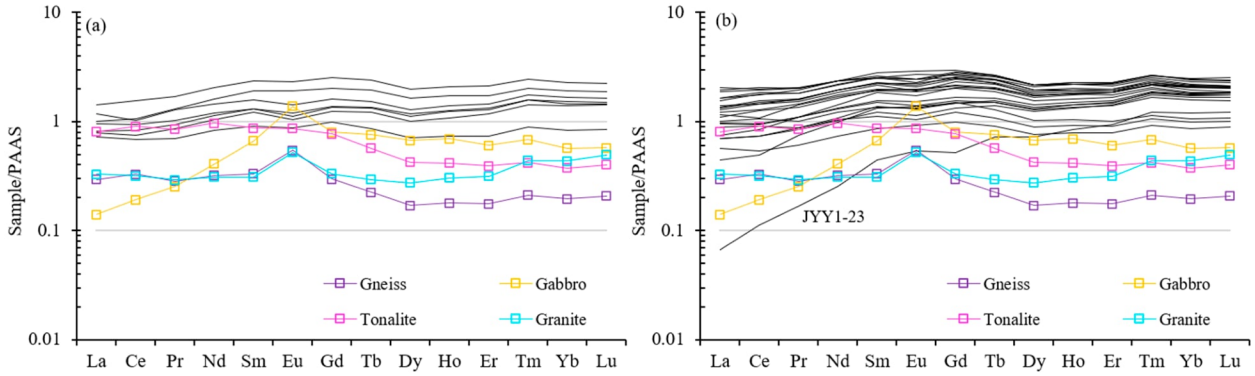


Figure 6. The spider diagram of REEs normalized by the PAAS for the of (**a**) the upper interval and (**b**) the lower interval in the Changling Sag. Each black polyline corresponds to one sample analyzed in this study. The reference data for potential parent rocks are derived from the Songliao Basin basement, which shares similar lithological characteristics with the surrounding Zhangguangcai, Great Xing'an, and Lesser Xing'an Ranges [35].

Table 5. The calculated paleoenvironmental proxies for the JYY1 well in the Member I.

Interval	Sample No.	Depth (m)	Paleoclimate			Redox Condition		Paleosalinity		Detrital Input			Paleoproductivity		
			CIA	CIA_C	τNa	V/Cr	Mo/Al	Sr/Ba	B/Ga	Ti/Al	Zr/Rb	Si/Al	P/Al	Ba/Al	Cu/Al
Upper interval	JYY1-3	2422.4	67	83.9	−0.80	1.40	1.21	0.60	4.48	0.040	6.2	3.0	0.012	0.004	0.0004
	JYY1-4	2425.4	62	82.1	−0.82	1.60	1.47	0.75	5.43	0.039	4.6	3.2	0.008	0.005	0.0005
	JYY1-32	2431.5	66	80.2	−0.78	1.62	1.27	0.75	6.66	0.042	5.9	3.2	0.008	0.003	0.0006
	JYY1-5	2433	64	80.0	−0.78	1.63	1.05	0.72	5.68	0.044	10.8	3.3	0.006	0.004	0.0006
	JYY1-7	2440.5	60	81.7	−0.83	1.96	1.86	1.34	6.58	0.044	16.4	3.1	0.008	0.003	0.0008
	JYY1-6	2448.6	61	80.2	−0.63	1.83	1.44	0.57	4.38	0.041	2.7	3.2	0.007	0.005	0.0004
	JYY1-8	2450	59	80.1	−0.77	1.21	1.15	0.64	3.22	0.042	2.7	3.5	0.006	0.010	0.0004
	Average		63	81.2	−0.77	1.61	1.35	0.77	5.20	0.042	7.0	3.2	0.008	0.005	0.0005
Lower interval	JYY1-9	2458.3	59	78.3	−0.80	0.97	0.43	0.47	5.27	0.047	18.4	3.2	0.012	0.004	0.0004
	JYY1-10	2459.3	56	76.1	−0.79	1.07	0.19	0.62	4.71	0.056	42.9	4.1	0.011	0.003	0.0004
	JYY1-2	2463	52	75.9	−0.83	0.86	0.42	1.55	3.83	0.048	9.0	4.6	0.008	0.005	0.0004
	JYY1-25	2465.5	62	82.7	−0.74	0.56	0.78	1.24	4.49	0.043	3.9	4.9	0.010	0.005	0.0004
	JYY1-11	2469.6	58	80.0	−0.64	1.73	1.18	0.90	3.77	0.042	3.1	3.3	0.007	0.004	0.0005
	JYY1-14	2470.6	59	81.5	−0.68	1.41	0.64	0.71	4.35	0.042	4.3	3.2	0.007	0.004	0.0004
	JYY1-12	2476.4	61	73.7	−0.81	1.42	1.48	0.81	4.33	0.045	2.0	3.4	0.008	0.007	0.0005
	JYY1-15	2479.4	67	81.9	−0.86	1.62	0.16	0.83	5.32	0.047	5.0	3.4	0.009	0.004	0.0005
	JYY1-13	2479.9	60	70.2	−0.88	0.79	0.36	0.74	4.61	0.046	12.2	3.0	0.010	0.005	0.0005
	JYY1-18	2483.1	64	80.2	−0.81	1.67	0.69	0.66	4.76	0.044	7.2	3.8	0.008	0.004	0.0005
	JYY1-16	2485.5	57	72.9	−0.81	1.21	0.71	0.97	4.86	0.045	6.5	3.4	0.009	0.005	0.0005
	JYY1-19	2490.6	66	84.0	−0.85	1.94	1.10	0.76	5.03	0.041	10.2	3.7	0.007	0.003	0.0005
	JYY1-22	2491.5	62	82.4	−0.84	1.28	1.13	1.10	5.28	0.044	8.4	3.2	0.010	0.003	0.0005
	JYY1-20	2494.2	65	84.1	−0.88	0.88	0.37	1.46	5.77	0.050	14.1	3.3	0.013	0.003	0.0007
	JYY1-23	2497.5	57	70.9	−0.85	0.91	0.41	0.81	6.12	0.053	38.4	3.0	0.012	0.002	0.0005
	JYY1-17	2499.8	63	71.9	−0.91	1.18	1.67	0.67	4.42	0.044	12.7	4.1	0.009	0.005	0.0005
	JYY1-21	2501.8	62	81.8	−0.83	1.56	0.90	0.89	5.78	0.045	10.5	3.6	0.009	0.003	0.0007
	JYY1-31	2509.8	62	81.9	−0.85	1.77	0.44	0.84	5.83	0.045	7.2	3.3	0.007	0.003	0.0005
	JYY1-26	2511.8	61	82.1	−0.86	1.27	0.35	1.02	4.51	0.049	3.0	3.4	0.008	0.005	0.0005
	JYY1-27	2514.6	64	81.8	−0.83	2.22	1.05	0.73	4.50	0.039	11.7	3.5	0.006	0.003	0.0004
	JYY1-28	2518	61	81.8	−0.85	1.51	0.44	0.84	4.62	0.048	13.8	3.2	0.009	0.004	0.0005
	JYY1-29	2520	63	82.7	−0.87	1.07	0.31	1.74	4.68	0.053	7.0	3.6	0.012	0.003	0.0006
	JYY1-30	2522.1	57	79.5	−0.82	1.25	0.65	1.59	3.87	0.045	6.7	3.6	0.014	0.004	0.0006
	Average		61	79.1	-0.82	1.31	0.69	0.95	4.81	0.046	11.2	3.7	0.009	0.004	0.0005

In summary, the provenance for the Member I remained generally stable. Both characteristics of Al_2O_3/TiO_2 ratios and PAAS-normalized REEs distribution indicate a pre-

dominantly felsic to intermediate provenance, broadly compatible with tonalitic source rocks. Consequently, the vertical variations observed in the geochemical proxies used in this study primarily reflect changes in paleoenvironment rather than shifts in sediment source composition. This interpretation provides a geochemical basis for reconstructing paleoenvironmental evolution and investigating the mechanisms controlling organic matter accumulation during the Member I deposition.

5.2. Paleoenvironment

5.2.1. Paleoclimate

Paleoclimate influences organic matter accumulation by regulating source-rock weathering, detrital input, and nutrient availability. The degree of chemical weathering was evaluated using the Chemical Index of Alteration (CIA) [39], calculated as follows:

$$CIA = [Al_2O_3 / (Al_2O_3 + CaO^* + Na_2O + K_2O)] \times 100\% \quad (2)$$

All oxide concentrations in this equation are expressed on a molar basis. CaO* denotes the CaO fraction associated with silicate minerals and was estimated using the correction procedure of [40]:

$$CaO^* = \begin{cases} CaO - \frac{10}{3}P_2O_5, & \text{if } CaO - \frac{10}{3}P_2O_5 < Na_2O \\ Na_2O, & \text{otherwise} \end{cases} \quad (3)$$

As chemical alteration intensifies, mobile elements such as Ca, Na, and K are progressively depleted relative to Al, leading to higher CIA values [39]. Conversely, lower values generally reflect less extensive alteration. For the Member I, CIA values vary between 52 and 67, averaging 61 (Table 5). The A–CN–K diagram was employed to examine weathering trends and post-depositional alteration (Figure 7a). The theoretical weathering trend proceeds from tonalite toward clay minerals, including kaolinite, gibbsite, and chlorite, approximately parallel to the A–CN side. Potassium metasomatism may facilitate the conversion of kaolinite to illite and plagioclase to K-feldspar, causing sample compositions to shift toward the K apex [41]. In Figure 7a, the samples define a trend that departs slightly from the ideal weathering trajectory, suggesting different degrees of K-metasomatism. Potassium alteration is more pronounced near the Al_2O_3 apex and weaker toward the CaO* + Na_2O apex. The CIA values were therefore adjusted along the dashed correction trajectories to obtain CIAc (Table 5). Corrected values range from 70.2 to 84.0, averaging 79.1 in the lower interval and 81.2 in the upper interval (Table 5).

The sodium depletion index (τNa) was also applied to assess weathering intensity, as it records Na loss associated with plagioclase alteration in granitic terrains [2,42]. It is defined as follows:

$$\tau Na = [(CNa, w \times CZr, p)/(CNa, p \times CZr, w)] - 1, \quad (4)$$

Here, C denotes the weight-based concentration of an element, and the subscripts w and p identify the weathered material and the corresponding parent rock, respectively [43]. Tonalite was selected as the reference composition because of its geochemical similarity to the Member I sediments. An average Na/Zr ratio of 244.8, derived from tonalitic rocks in the Zhangguangcai, Great Xing'an, and Lesser Xing'an Ranges, was adopted for calculating τNa [35]. Generally, τNa exhibits a negative correlation with weathering intensity [2], that is, lower τNa values correspond to stronger chemical weathering, whereas higher values indicate weaker weathering conditions. The Zr/Sc ratio was employed to indicate sedimentary recycling and hydraulic sorting [37]. τNa shows no obvious correlation with Zr/Sc in the upper interval with $R^2 = 0.0515$, indicating negligible influence from

hydraulic sorting (Figure 7b). With respect to the lower interval, τNa shows a very weak correlation with Zr/Sc with R^2 = 0.1064. Only three circled samples show high Zr/Sc ratios within this interval. In summary, τNa is weakly influenced by hydraulic sorting and sedimentary recycling.

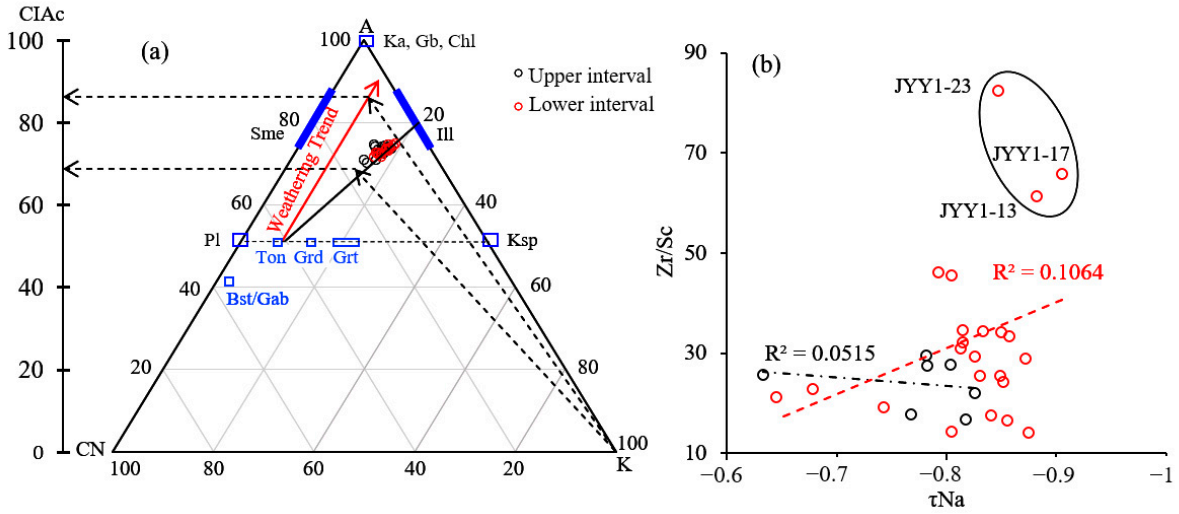


Figure 7. (**a**) A–CN–K diagram for the Member I samples from the JYY1 well after correction for excess K. The red solid arrow indicates the ideal tonalite weathering pathway; the blue hollow squares represent the ideal compositions of specific minerals and rocks; the thick blue lines indicate the compositional ranges of smectite and illite; the black solid line represents the actual weathering trend, whereas the black dashed arrows represent the CIA correction directions [41]. CIA_C = corrected CIA, A = Al_2O_3, CN = CaO* + Na_2O, K = K_2O, Ka = Kaolinite, Gb = Gibbsite, Chl = Chlorite, Pl = Plagioclase, Ksp = K-Feldspar, Sme = Smectite, Ill = Illite, Bst/Gab = basalt/gabbro, Ton = tonalite, Grd = granodiorite, Grt = granite. (**b**) Correlation diagram between τNa and Zr/Sc for the Member I samples of the JYY1 well.

After excluding the three anomalous samples, mean CIAc and τNa values are 80 and −0.81 for the lower interval, compared with 81.2 and −0.77 for the upper interval. A humid subtropical to tropical climate during the Member I deposition is supported by low ostracod $\delta^{18}O$ values [44] and vegetation records dominated by broad-leaved evergreens rather than conifers [45]. In addition, $\delta^{26}Mg$ indicates a rainfall-driven lake flooding event during lower-interval deposition [46], consistent with the pronounced Na depletion observed here. Because CIAc differs only slightly between the two intervals, τNa provides a clearer indication of their relative weathering conditions. Considering that more samples in the lower interval contain more silt-grain particles and develop clear wavy and horizontal beddings (Figure 2d–f), we tend to attribute the high Zr/Sc ratios to hydraulic sorting. The lower interval is therefore interpreted to have experienced greater precipitation and stronger hydrodynamic activity, whereas the upper interval reflects relatively reduced rainfall and calmer depositional conditions.

5.2.2. Redox Conditions

The concentrations of redox-sensitive elements, such as Mo, U, Ni, V, Cu, and Co, can offer insights into oxygen availability during deposition [47–50]. Under oxic conditions, sedimentary V is mainly associated with detrital material and generally occurs at low concentrations. As oxygen availability declines, V(V) can be reduced to V(IV) or V(III), promoting its accumulation through interactions with organic matter, precipitation as poorly soluble hydroxides, and formation of organic complexes [50]. In contrast to V, Cr has a limited tendency to precipitate as insoluble sulfides and can be released back into

the water column as organic matter decomposes. Therefore, the Cr content in sediments is mainly controlled by detrital inputs [50]. An increase in V/Cr may consequently indicate enhanced authigenic V enrichment under more reducing conditions. In oxygenated waters, Mo predominantly occurs as dissolved molybdate and has limited affinity for particulate phases, leading to low sedimentary Mo accumulation [51]. Under anoxic conditions, Mo retention can be enhanced through interactions with organic thiomolybdates and iron sulfides [52]. Accordingly, higher Mo/Al ratios may reflect more reducing depositional environments.

Algeo and Liu [53] suggested that variations in terrigenous detritus input among different sedimentary basins may lead to differing redox classification thresholds, yet the inflection point where two independent proxies concurrently show an increasing trend can be taken as the boundary between oxic (or possibly anoxic) and anoxic environments. As shown in Figure 8, a positive correlation exists between the two proxies when V/Cr > 1.4 and Mo/Al > 1.0, with $R^2 = 0.54$ for the upper interval of Member I. Therefore, V/Cr = 1.4 and Mo/Al = 1.0 are determined as the thresholds between possibly anoxic and anoxic conditions. Vertically, the average V/Cr is 1.31 in the lower interval of the Member I, and increases to 1.61 in the upper interval (Table 4), indicating a higher enrichment of authigenic V in the upper interval. Both the V/Cr and Mo/Al proxies consistently demonstrate that the upper interval was deposited in anoxic conditions.

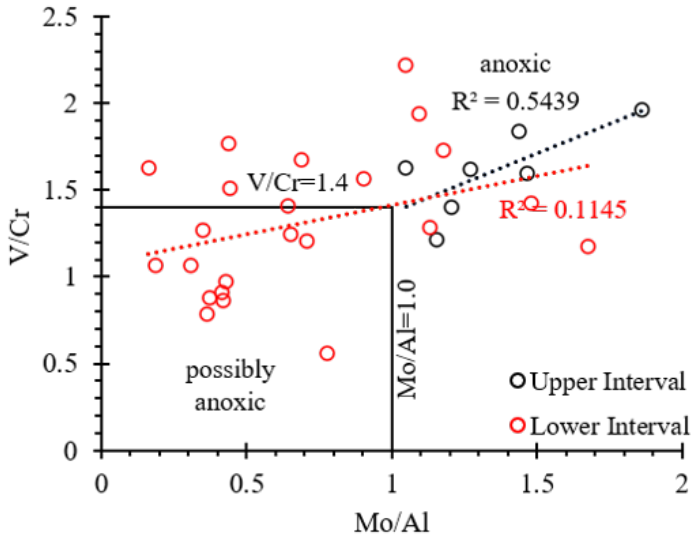


Figure 8. Bivariate analysis showing the relationships of Mo/Al versus V/Cr for the Member I shale in the Changling Sag.

Iron speciation was further used to evaluate redox conditions and potential microbial respiration pathways. Commonly applied Fe_{HR}/Fe_T criteria distinguish anoxic (>0.38), potentially anoxic (0.22–0.38), and oxic (<0.22) settings [30,54]. The proportion of pyrite-bound iron also provides information on water-column chemistry: Fe_{py}/Fe_{HR} values above approximately 0.7–0.8 are generally associated with euxinia, whereas lower ratios are consistent with ferruginous conditions [55]. For lacustrine shales, Zhang et al. and Li et al. proposed additional Fe_{py}/Fe_{HR} ranges to infer dominant respiration pathways: 0.5–0.8 for bacterial sulfate reduction (BSR), below 0.15 for dissimilatory iron reduction (DIR), and 0.15–0.5 for their combined influence [3,56]. Mean Fe_{HR}/Fe_T ratios increase from 0.39 in the lower interval to 0.45 in the upper interval, accompanied by an increase in Fe_{py}/Fe_{HR} from 0.27 to 0.50 (Table 2). Therefore, the lower interval is dominated by ferruginous conditions, under which DIR is the prevailing microbial respiration pathway. By contrast, BSR becomes more important in the upper interval (Figure 9). This conclusion is further

supported by the elevated HI values in the upper interval (Figure 10), as increased BSR activity would produce H_2S, which is toxic to methanogens and microorganisms involved in DIR [57], thereby inhibiting their organic matter mineralization and ultimately leading to better preservation of hydrogen-rich organic components [3].

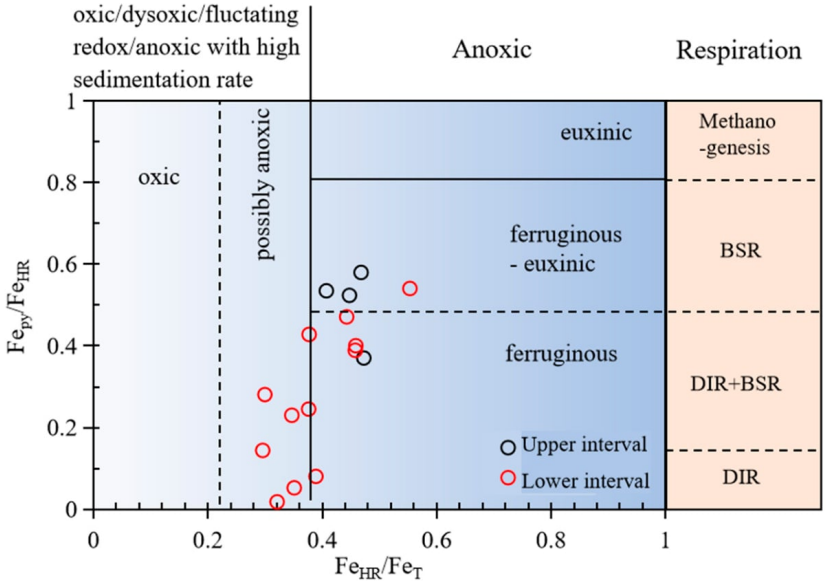


Figure 9. Iron-speciation characteristics of the Member I shale in the Changling Sag, with redox and microbial respiration fields defined according to Raiswell et al. [31] and Li et al. [3].

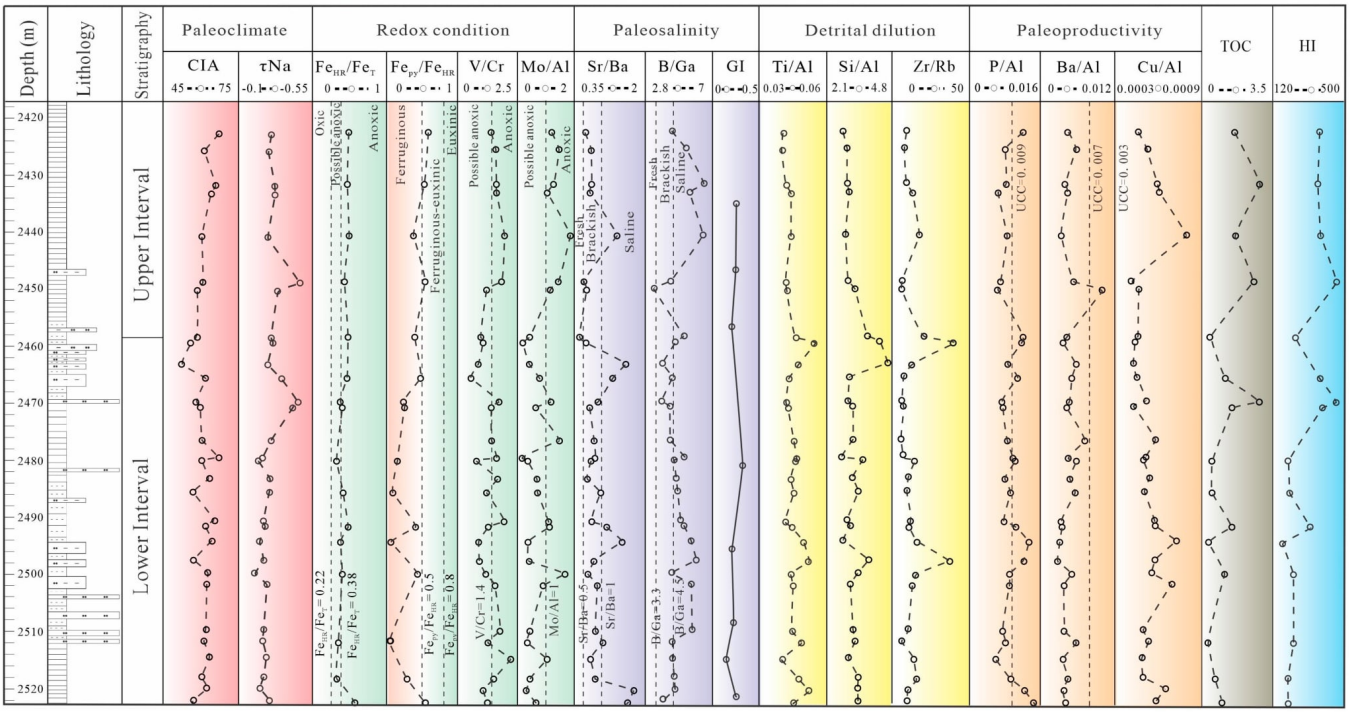


Figure 10. Paleoclimatic and paleoenvironmental oscillations of the Member I shale in the Changling Sag. Dashed lines are based on the results of this study, and solid lines represent GI data from [16].

5.2.3. Paleosalinity

Differences in the geochemical behavior of Sr and Ba provide the basis for using their ratio as a paleosalinity proxy. Although both elements can remain dissolved in freshwater,

increasing salinity promotes the precipitation of Ba as $BaSO_4$, while Sr tends to remain in solution until salinity reaches higher levels [58,59]. Sr/Ba values above 1.0, between 0.5 and 1.0, and below 0.5 have previously been associated with saline, brackish, and freshwater settings, respectively [59]. In the Member I shale, Sr/Ba varies between 0.47 and 1.74, averaging 0.91. Only sample JYY1-9 has a ratio below 0.5 (0.47; Table 5). These values generally indicate brackish to saline depositional conditions. The lower interval exhibits a higher average Sr/Ba ratio (0.95) than the upper interval (0.77), possibly suggesting elevated salinity during deposition of the lower interval.

Boron uptake by clay minerals is influenced by its concentration in the surrounding water, providing a basis for using sedimentary B as a salinity indicator [60,61]. The B/Ga ratio further exploits the contrasting mobility of these elements: dissolved borate is relatively mobile, whereas Ga is less readily transported. As a result, higher B/Ga ratios have been interpreted as reflecting increased paleosalinity [62]. Wang et al. proposed B/Ga ranges of below 3.0–3.3, 3.3–4.5, and above 4.5–5 for freshwater, brackish, and saline conditions, respectively [63]. Among the JYY1 samples, only JYY1-8 has a B/Ga ratio of 3.22, indicating a freshwater environment. Mean B/Ga values are 5.20 in the upper interval and 4.81 in the lower interval (Table 5). This upward increase is consistent with the higher Gammacerane Index (GI) reported for the upper interval of the Member I in the Changling Sag [16] (Figure 10), suggesting a relative increase in salinity.

5.2.4. Detrital Dilution

The input of terrigenous detritus into sediments may dilute their organic matter content. In fine-grained sediments, Al is largely associated with aluminosilicates, particularly clays and feldspars, whereas Ti and Zr are frequently associated with relatively coarse detrital particles or heavy minerals, including rutile and zircon [64]. In contrast, Rubidium tends to be enriched in clay minerals [64]. These contrasting mineral associations allow Ti/Al and Zr/Rb to reflect variations in grain size, hydraulic sorting, and detrital composition [65,66]. For the Member I shale from the JYY1 well, Ti/Al ratios span 0.039–0.056 with averages of 0.046 in the lower interval and 0.042 in the upper interval (Table 5; Figure 10). Zr/Rb spans 2.03–42.90 and shows an average of 11.2 in the lower interval compared with 7.0 in the upper interval (Table 4).

Si/Al was additionally examined to help distinguish the effects of mineral composition and grain size on Ti/Al and Zr/Rb. Within shale succession, Si is predominantly hosted by quartz, feldspars, and clay minerals, whereas Al is mainly associated with feldspars and clay minerals. K-feldspar and albite have Si/Al atomic ratios of approximately 3, compared with 1–1.7 for common clay minerals such as illite and smectite [67,68]. Accordingly, elevated Si/Al values may indicate a greater relative contribution from coarser clastic minerals, including quartz and feldspar. Typical muddy siltstones from well JYY1 (e.g., JYY1-13, JYY1-23, and JYY1-9) exhibit Si/Al values of 3.85, 4.12, and 4.06, respectively, exceeding those of the other shale samples. This contrast supports the use of Si/Al to distinguish the relative contributions of coarse clastic minerals and fine-grained clay components in the Member I. Comparable vertical trends are observed for Si/Al, Ti/Al, and Zr/Rb, all of which exhibit higher average values in the lower interval relative to the upper interval (Figure 10; Table 4). These differences suggest a larger proportion of silt-sized detritus and a stronger dilution effect in the lower interval. The occurrence of wavy and horizontal bedding, together with its relatively lighter rock color (Figure 2), further supports deposition under higher-energy hydrodynamic conditions.

5.2.5. Paleoproductivity

Organic matter accumulation is partly influenced by primary productivity, which can be assessed using geochemical proxies, particularly phosphorus (P) and barium (Ba). Phosphorus supports algal growth and may provide information on productivity in the water column [69,70]. Barium is associated with sinking biogenic particles, and its accumulation in sediments has been used to infer productivity [71]. To reduce the influence of detrital contributions, P and Ba concentrations were normalized to Al [71,72]. However, both elements may be remobilized under anoxic conditions, potentially affecting their preservation in sediments [50]. Cu/Al was therefore included as an additional indicator because Cu can be transported with organic matter and subsequently retained in pyrite during organic matter degradation under anoxic conditions [50].

The Member I samples have P/Al ratios of 0.006–0.014, close to the UCC value of 0.009. Mean P/Al values are 0.008 for the upper interval and 0.009 for the lower interval (Table 4). Ba/Al is generally below the UCC value of 0.007, except in JYY1-8 (0.010), indicating overall Ba depletion. The upper interval has a slightly higher mean Ba/Al ratio (0.005) than the lower interval (0.004; Table 4). Both intervals have an identical mean Cu/Al ratio of 0.0005. The relatively small stratigraphic variations in these three proxies may suggest that paleoproductivity did not change substantially during the Member I deposition in the Changling Sag.

5.3. Accumulation Mechanism for Organic Matter

5.3.1. Controlling Factors for Organic Matter Accumulation

The enrichment of organic matter involves multiple interacting processes. In this study, statistical analysis was conducted to assess its controlling factors. Specifically, 16 valid samples from the Member I of the JYY1 well were analyzed using Origin 2021 to generate a correlation heatmap. A total of 14 variables, including TOC and geochemical parameters representing paleoclimate, paleoproductivity, redox conditions, paleosalinity, and detrital dilution, were subjected to a two-tailed Pearson correlation analysis. This analysis evaluated the magnitude and direction of linear associations between environmental parameters and TOC. Pearson's correlation coefficient (r) served to quantify these associations, while *p*-values were obtained via two-tailed significance testing, with statistical significance defined at $p < 0.05$.

The statistical results suggest that oxygen-depleted bottom-water conditions played an important role in preserving organic matter (Figure 11). Positive correlations with TOC are observed for Mo/Al, V/Cr, and Fe_{py}/Fe_{HR}, with respective r values of 0.69, 0.67, and 0.54 ($p = 0.003$, 0.004, and 0.03, respectively). This indicates that the anoxic conditions, specifically the ferruginous condition, effectively restricted the oxidative decomposition of organic matter, acting as the most critical factor for its preservation. In comparison, Cu/Al ($r = -0.06$, $p = 0.84$), P/Al ($r = -0.51$, $p = 0.04$), and Ba/Al ($r = -0.17$, $p = 0.54$) do not exhibit statistically significant positive associations with TOC. These results suggest that primary productivity was unlikely to be the dominant controlling factor for organic matter accumulation in the study area. TOC is strongly negatively correlated with Ti/Al ($r = -0.82$, $p = 0.0001$), consistent with dilution by silt-rich detritus. A positive TOC–τNa relationship ($r = 0.69$, $p = 0.003$) further suggests that relatively reduced precipitation may have facilitated organic matter accumulation. Taken together, the results support a preservation-dominated accumulation pattern, with detrital dilution acting as an additional negative influence.

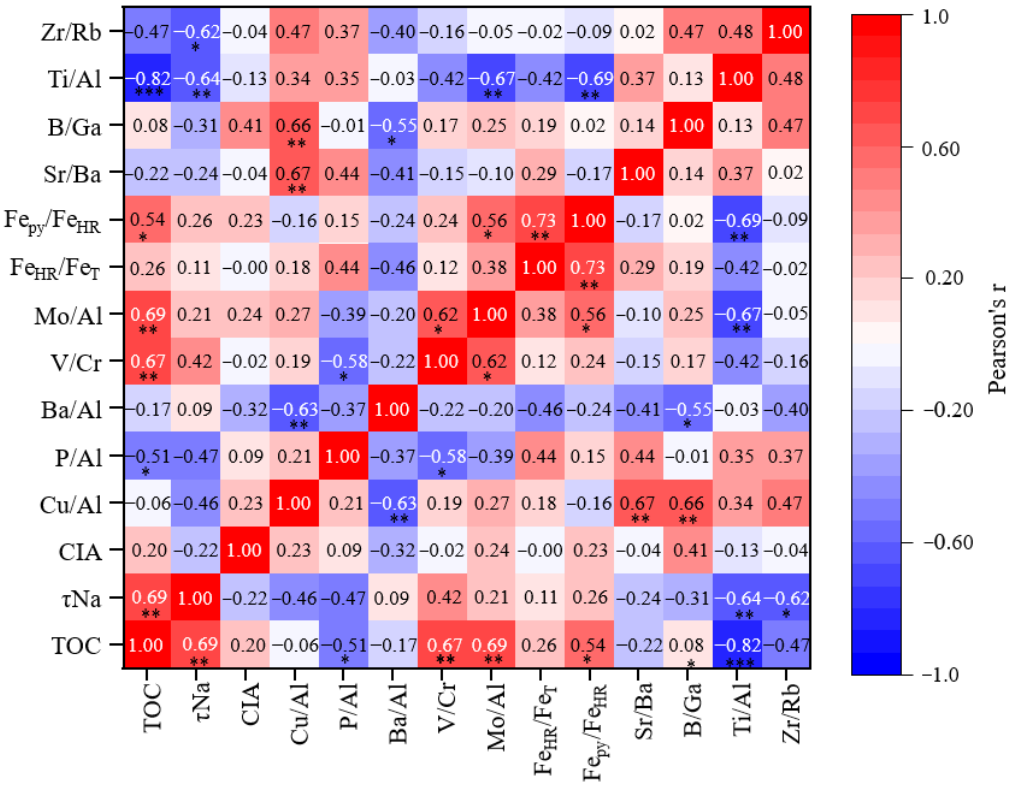


Figure 11. Pearson correlation heatmap of TOC and paleoenvironmental proxies for the Member I samples from the JYY1 well. Statistical significance is indicated by *, **, and ***, corresponding to $p < 0.05$, $p < 0.01$, and $p < 0.001$, respectively.

5.3.2. Accumulation Model for Organic Matter

A conceptual model was developed to illustrate organic matter accumulation in the Member I of the Changling Sag (Figure 12).

The lower interval (stage a) is a high precipitation and strong runoff period. During this stage, the climate was humid, and heavy precipitation led to an elevated riverine input (Figure 12a). This diluted the lacustrine water column to brackish conditions and markedly enhanced the hydrodynamic energy. Intensified hydrodynamic activity weakened water-column stratification and enhanced vertical mixing of oxygen-rich waters, resulting in elevated oxygenation of the bottom water, with only localized development of ferruginous conditions. In this type of water column, organic matter was largely degraded by aerobic microbes in overlying oxic water, and further decomposed by prevailing DIR in the ferruginous bottom water [3,56]. Under this scenario, euhedral and framboidal pyrite formation was only formed in pore waters beneath the sediment–water interface. Meanwhile, runoff supplied abundant coarse detrital particles, particularly silt, which reduced the relative abundance of organic matter in the sediments through dilution. Together, these processes limited organic matter enrichment during Stage a.

The upper interval (stage b) is a low precipitation and weak runoff period. At this stage, both precipitation and riverine influx declined, resulting in a weak hydrodynamic lake with a brackish to saline water column. Under such a relatively stable water column structure, a well-developed redox stratification was prone to form, resulting in an enlarged ferruginous-euxinic bottom water and a thinner overlying oxic water. Therefore, organic matter was better preserved due to the inhibited oxidative degradation. Meanwhile, increased BSR in the ferruginous-euxinic bottom water could release toxic H_2S to suppress DIR and methanogenesis, which also promoted organic matter preservation [3]. Framboidal and euhedral pyrites formed in both bottom and pore waters. Additionally, fine-grained sediment such

as clay minerals could also adsorb organic matter and protect it from oxidation or microbial alteration [17,73]. The combined effects of water-column stratification, reducing conditions, and mineral-associated protection favored organic matter accumulation during Stage b.

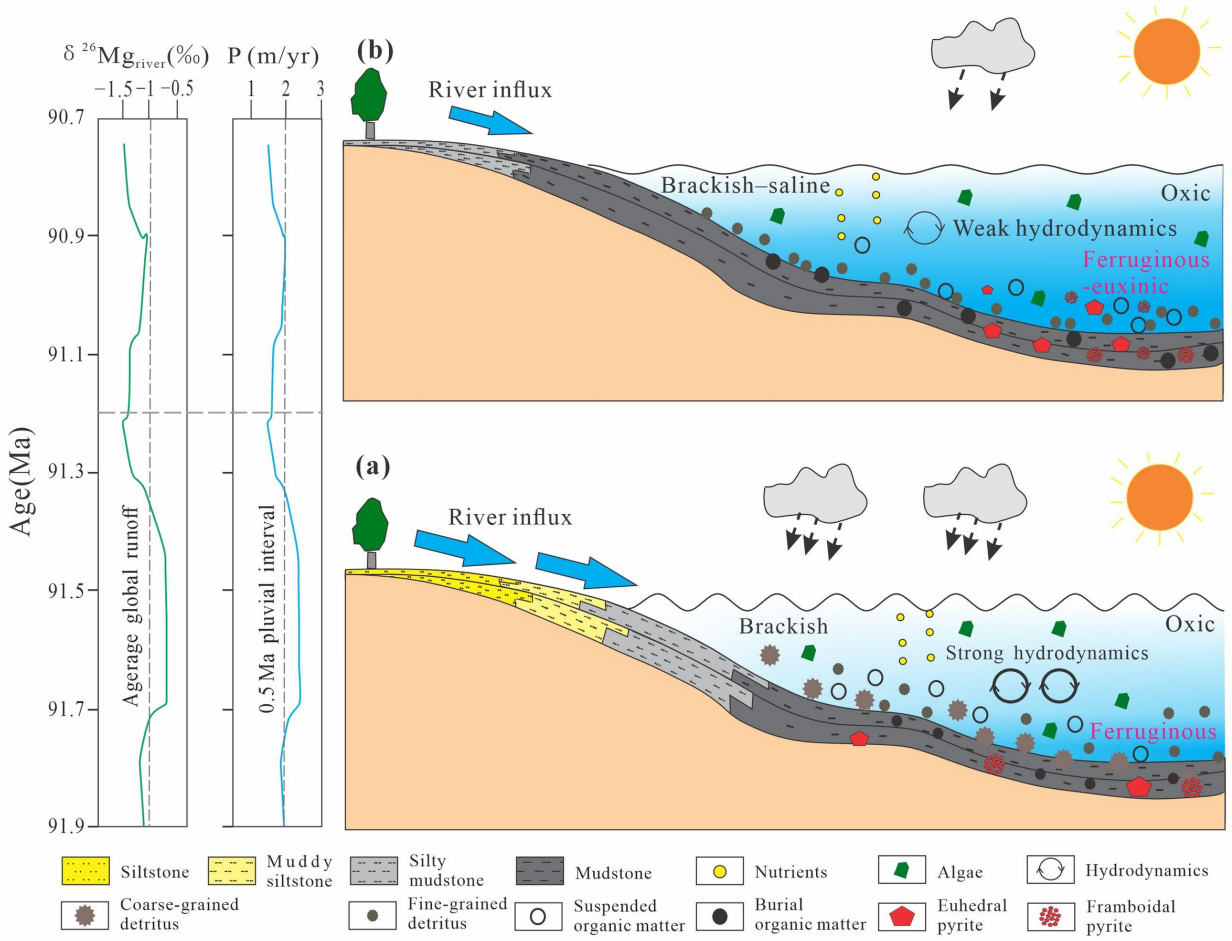


Figure 12. Conceptual model depicting the organic matter enrichment processes in the lower (**a**) and upper (**b**) intervals of the Member I lacustrine shale from the Changling Sag. The δ^{26}Mg-based reconstruction of mean annual precipitation (P, m/yr) during the Member I deposition (91.9–90.7 Ma) is from Liu et al. [46].

6. Conclusions

(1) Evidence from Al_2O_3/TiO_2 ratios and PAAS-normalized REEs patterns suggests that the Member I sediments in the Changling Sag were mainly derived from felsic to intermediate source rocks, with geochemical characteristics broadly consistent with tonalite.

(2) The Member I deposition in the Changling Sag occurred under a humid subtropical to tropical climate, accompanied by moderate to strong chemical weathering and generally brackish-to-saline lake conditions. During lower-interval deposition, greater precipitation and riverine input promoted vigorous water circulation in a brackish, ferruginous lake. In contrast, reduced rainfall and fluvial supply during upper-interval deposition favored weaker hydrodynamic activity and the development of brackish-to-saline, ferruginous–euxinic conditions.

(3) The enrichment of organic matter in the Member I was primarily governed by preservation conditions and detrital dilution. Higher TOC in the upper interval was favored by the expansion of ferruginous–euxinic bottom waters, reduced silt-sized detrital contributions, and enhanced organic matter retention by clay minerals. In the lower interval, greater

silt input and less favorable preservation conditions limited organic carbon accumulation. The occurrence of abundant pyrite and elevated Fe_{py}/Fe_{HR} ratios may therefore provide supplementary evidence for identifying organic-rich shale intervals with shale oil and gas potential.

Author Contributions: All authors contributed to the study conception and design. writing—original draft preparation, L.L.; writing—review and editing, H.L. and B.L.; data curation, X.W. and Z.J.; funding acquisition, B.W. and J.Y.; formal analysis, Y.F.; methodology, F.X. and L.C. All authors have read and agreed to the published version of the manuscript.

Funding: This research was funded by the National Natural Science Foundation(U2244207, 42202153), Program of Heilongjiang Province (YQ2024D005, TY24001), and Basic Research Support Program for Outstanding Young Faculty of Heilongjiang Province (YQJH2023089).

Data Availability Statement: The data supporting the findings of this study are provided within the article.

Acknowledgments: The authors sincerely appreciate the constructive comments and suggestions provided by the editors and anonymous reviewers, which helped improve the clarity and overall quality of this manuscript.

Conflicts of Interest: The authors declare no conflicts of interest.

Appendix A

Table A1. Rare earth elemental compositions and calculations for the JYY1 well in Member I, all in μg/g content.

Interval	Sample No.	Depth (m)	La	Ce	Pr	Nd	Sm	Eu	Gd	Tb	Dy	Y	Ho	Er	Tm	Yb	Lu	$(La/Yb)_N$	REE	Eu/Eu*
Upper interval	JYY1-3	2422.4	30	59	9	33	7	1.2	6	0.9	5	23	1.1	3.6	0.6	3.9	0.6	0.6	184	0.85
	JYY1-4	2425.4	44	82	13	46	9	1.6	8	1.2	7	35	1.5	4.5	0.7	4.6	0.7	0.7	259	0.90
	JYY1-32	2431.5	37	75	10	38	7	1.2	6	1.0	6	29	1.3	3.9	0.6	4.0	0.6	0.7	221	0.84
	JYY1-5	2433	31	66	10	37	7	1.3	7	1.1	6	27	1.3	4.1	0.6	4.3	0.7	0.5	204	0.90
	JYY1-7	2440.5	54	125	17	66	13	2.6	12	1.8	11	46	2.2	6.6	1.0	6.4	1.0	0.6	365	0.96
	JYY1-6	2448.6	28	55	7	27	5	1.0	5	0.7	4		0.8	2.3	0.4	2.3	0.4	0.9	137	0.93
	JYY1-8	2450	38	85	13	51	11	2.1	10	1.5	9	34	1.8	5.3	0.8	5.3	0.8	0.5	268	0.97
	Average		37	78	11	43	8	1.6	7	1.2	7	32	1.4	4.3	0.7	4.4	0.7	0.7	234	0.91
Lower interval	JYY1-9	2458.3	17	39	8	31	7	1.5	7	1.2	7	28	1.5	4.6	0.7	4.8	0.8	0.3	159	0.99
	JYY1-10	2459.3	29	67	11	45	10	1.9	10	1.6	9	39	1.9	5.6	0.9	5.7	0.9	0.4	239	0.88
	JYY1-2	2463	53	116	16	62	13	2.5	12	1.8	10	50	2.1	6.1	0.9	5.8	0.9	0.7	352	0.95
	JYY1-25	2465.5	38	84	10	39	8	1.5	7	1.0	5		1.1	3.1	0.5	3.0	0.5	1.0	202	0.94
	JYY1-11	2469.6	34	73	9	33	6	1.1	6	0.8	5		1.0	2.8	0.4	2.8	0.4	0.9	175	0.80
	JYY1-14	2470.6	21	43	6	24	5	1.0	5	0.7	4		0.8	2.4	0.4	2.4	0.4	0.7	116	0.99
	JYY1-12	2476.4	78	158	21	75	14	2.7	12	1.7	9	43	1.9	5.4	0.8	5.2	0.8	1.1	428	0.97
	JYY1-15	2479.4	59	144	19	70	14	2.5	13	2.0	11	46	2.4	7.0	1.1	6.8	1.0	0.6	399	0.86
	JYY1-13	2479.9	50	120	16	62	13	2.4	12	1.9	11	46	2.3	6.9	1.0	7.0	1.1	0.5	354	0.89
	JYY1-18	2483.1	36	75	11	42	9	1.7	8	1.3	8	35	1.6	4.8	0.8	5.0	0.8	0.5	239	0.94
	JYY1-16	2485.5	52	124	16	62	13	2.3	11	1.8	10	45	2.1	6.1	0.9	6.1	0.9	0.6	353	0.90
	JYY1-19	2490.6	26	59	9	33	7	1.2	6	1.1	7	28	1.4	4.4	0.7	4.7	0.7	0.4	187	0.89
	JYY1-22	2491.5	44	87	14	54	11	2.1	9	1.4	8	42	1.7	5.2	0.8	5.1	0.8	0.6	286	0.95
	JYY1-20	2494.2	63	141	20	76	16	3.2	14	2.1	11	49	2.3	6.6	1.0	6.2	0.9	0.8	411	1.01
	JYY1-23	2497.5	3	9	2	8	2	0.6	2	0.6	4	10	0.9	2.9	0.5	3.4	0.5	0.1	49	1.11
	JYY1-17	2499.8	46	103	15	56	11	2.1	10	1.5	9	43	1.8	5.7	0.9	5.9	0.9	0.6	311	0.95
	JYY1-21	2501.8	37	77	11	41	8	1.6	7	1.2	7	34	1.4	4.3	0.7	4.4	0.7	0.6	237	0.93
	JYY1-31	2509.8	49	117	16	59	12	2.1	11	1.7	10	43	2.0	5.9	0.9	6.0	0.9	0.6	334	0.85
	JYY1-26	2511.8	74	163	21	75	15	2.7	13	2.0	12	58	2.4	7.0	1.1	6.7	1.0	0.8	453	0.89
	JYY1-27	2514.6	26	59	9	35	8	1.4	7	1.2	7	30	1.5	4.6	0.7	4.9	0.8	0.4	196	0.92
	JYY1-28	2518	42	101	14	52	11	2.2	10	1.6	9	41	1.9	5.7	0.9	5.8	0.9	0.5	299	0.97
	JYY1-29	2520	71	156	20	75	14	3.0	13	1.9	10	46	2.1	5.9	0.9	5.5	0.8	1.0	426	1.03
	JYY1-30	2522.1	62	148	18	70	14	2.7	13	2.0	11	53	2.3	6.7	1.0	6.5	1.0	0.7	412	0.93
	Average		44	98	14	51	10	2.0	9	1.5	9	41	1.8	5.2	0.8	5.2	0.8	0.6	288	0.94

References

1. Alipour, M. Hydrocarbon source rocks. In *Basics of Petroleum Geochemistry: With Examples from the Zagros Fold and Thrust Belt of Iran*; Springer Nature: Cham, Switzerland, 2025; pp. 3–18.
2. Li, H.X.; Liu, B.; Jiang, Q.C.; Xu, C.L.; Wang, Z.G.; Awan, R.S.; Lu, H.F.; Guo, L. Elemental geochemistry of the Aalenian (Middle Jurassic) shales from the northeastern Sichuan Basin: Evidence for provenance, climate oscillations and organic matter accumulation mechanism. *Mar. Pet. Geol.* **2025**, *180*, 107485. [CrossRef]
3. Li, H.X.; Jiang, Z.; Liu, B.; Yang, J.G.; Xiao, F.; Li, S.C.; Huang, Y.M. Influence of DIR and BSR in organic carbon preservation and mineralization: Insights from low-sulfate shale of the first member of the Qingshankou Formation. *Mar. Geosci. Energy Resour.* **2026**, *189*, 207731. [CrossRef]
4. Ma, Y.; Feng, J. Depositional environment variations and organic matter accumulation of the first member of the Qingshankou formation in the southern Songliao Basin, China. *Front. Earth Sci.* **2023**, *11*, 1249787. [CrossRef]
5. Dong, T.; He, S.; Yin, S.Y.; Wang, D.X.; Hou, Y.G.; Guo, J.G. Geochemical characterization of source rocks and crude oils in the Upper Cretaceous Qingshankou Formation, Changling Sag, southern Songliao Basin. *Mar. Pet. Geol.* **2015**, *64*, 173–188. [CrossRef]
6. Yuan, W.; Liu, G.D.; Zhou, X.X.; Xu, L.M.; Li, C.Z. Palaeoproductivity and organic matter accumulation during the deposition of the Chang 7 organic-rich shale of the Upper Triassic Yanchang Formation, Ordos Basin, China. *Geol. J.* **2020**, *55*, 3139–3156. [CrossRef]
7. Xu, Z.; Wang, Y.; Jiang, S.; Fang, C.; Liu, L.; Wu, K.; Luo, Q.; Li, X.; Chen, Y. Impact of input, preservation and dilution on organic matter enrichment in lacustrine rift basin: A case study of lacustrine shale in Dehui Depression of Songliao Basin, NE China. *Mar. Pet. Geol.* **2022**, *135*, 105386. [CrossRef]
8. Hu, T.; Pang, X.; Jiang, S.; Wang, Q.; Xu, T.; Lu, K. Impact of paleosalinity, dilution, redox, and paleoproductivity on organic matter enrichment in a saline lacustrine rift basin: A case study of Paleogene organic-rich shale in Dongpu Depression, Bohai Bay Basin, Eastern China. *Energy Fuels* **2018**, *32*, 5045–5061. [CrossRef]
9. Cheng, L.J.; Jia, J.L.; Liu, B.; Fu, X.F.; Li, H.X.; Xing, J.L.; Guan, J.Y. Quantitative comparison of the main controlling factors of organic matter enrichment in shore-shallow lacustrine and deep lacustrine shales: A case study of the first member of the Qingshankou Formation in the Changling Sag, Songliao Basin. *Acta Geol. Sin.* **2024**, *98*, 3773–3787. (In Chinese)
10. Xiao, Z.L.; Chen, S.J.; Zhang, S.M.; Zhang, R.; Zhu, Z.Y.; Lu, J.G.; Li, Y.; Yin, X.D.; Tang, L.X.; Liu, Z.H.; et al. Sedimentary environment and model for lacustrine organic matter enrichment: Lacustrine shale of the Early Jurassic Da'anzhai Formation, central Sichuan Basin, China. *J. Palaeogeogr.* **2021**, *10*, 584–601. [CrossRef]
11. Wang, Q.; Jiang, F.; Ji, H.; Jiang, S.; Liu, X.; Zhao, Z.; Wu, Y.; Xiong, H.; Li, Y.; Wang, Z. Effects of paleosedimentary environment on organic matter enrichment in a saline lacustrine rift basin—A case study of Paleogene source rock in the Dongpu Depression, Bohai Bay Basin. *J. Pet. Sci. Eng.* **2020**, *195*, 107658. [CrossRef]
12. Peng, J.W.; Hu, Z.Q.; Feng, D.J.; Wang, Q.R. Variations of organic matter content and type within the sequence stratigraphic framework of the lacustrine deep-water Dongyuemiao formation, Sichuan Basin, Western China. *Mar. Pet. Geol.* **2023**, *149*, 106104. [CrossRef]
13. Hu, C.X.; Yang, S.; Lu, Y.C.; Du, X.B. Development characteristics of multi-cycle slope-break geomorphology and its control on depositional processes in the Changling Sag. *Pet. Geol. Exp.* **2013**, *35*, 17–23. (In Chinese)
14. Bai, J.; Xu, X.Y.; Chen, S.; Liu, W.B.; Liu, C.; Zhang, C.S. Sedimentary facies characteristics and paleoenvironment reconstruction of the first member of the Qingshankou Formation in the Qian'an area, Changling Sag, Songliao Basin: A case study of Well Jiyeyou 1. *Geol. China* **2020**, *47*, 220–235. (In Chinese)
15. Wang, A.; Hu, M.Y.; Gao, J.J.; Yang, L.; Xing, J.L. Element geochemical characteristics and paleoenvironmental significance of mud shale in the first member of the Qingshankou Formation, Changling Sag, southern Songliao Basin. *J. Jilin Univ. Earth Sci. Ed.* **2024**, *54*, 2075–2088.
16. Meng, Q.T.; Zhang, X.; Yang, L.; Gao, J.J.; Liu, Z.J.; Hu, F.; Xing, J.L.; Zhang, C.M.; Kang, J.N.; Cui, B.; et al. Organic matter enrichment mechanism of fine-grained sediments in continental depression lacustrine basins: A case study of the Qingshankou Formation in the Changling Sag, Songliao Basin. *J. Palaeogeogr.* **2024**, *26*, 401–415. (In Chinese)
17. Li, L.; Bao, Z.; Li, L.; Li, Z.; Ban, S.; Li, Z.; Wang, T.; Li, Y.; Zheng, N.; Zhao, C.; et al. The source and preservation of lacustrine shale organic matter: Insights from the Qingshankou Formation in the Changling Sag, Southern Songliao Basin, China. *Sediment. Geol.* **2024**, *466*, 106649. [CrossRef]
18. Zhang, P.L.; Xu, Y.B.; Meng, Q.T.; Liu, Z.J.; Zhang, J.Q.; Shen, L.; Zhang, S.H. Sequence stratigraphy and geochemistry of oil shale deposits in the Upper Cretaceous Qingshankou Formation of the Songliao Basin, NE China: Implications for the geological optimization of in situ oil shale conversion processing. *Energies* **2020**, *13*, 2964. [CrossRef]
19. Sorokin, A.P.; Malyshev, Y.F.; Kaplun, V.B.; Sorokina, A.T.; Artemenko, T.V. Evolution and deep structure of the Zeya-Bureya and Songliao sedimentary basins (East Asia). *Russ. J. Pac. Geol.* **2013**, *7*, 77–91. [CrossRef]

20. Wang, T.T.; Ramezani, J.; Wang, C.S.; Wu, H.C.; He, H.Y.; Bowring, S.A. High precision U-Pb geochronologic constraints on the Late Cretaceous terrestrial cyclostratigraphy and geomagnetic polarity from the Songliao Basin, Northeast China. *Earth Planet. Sci. Lett.* **2016**, *446*, 37–44. [CrossRef]
21. Liu, B.; Sun, J.H.; Zhang, Y.Q.; He, J.L.; Fu, X.F.; Yang, L.; Xing, J.L.; Zhao, X.Q. Reservoir space and enrichment model of shale oil in the first member of Cretaceous Qingshankou Formation in the Changling Sag, southern Songliao Basin, NE China. *Pet. Explor. Dev.* **2021**, *48*, 608–624. [CrossRef]
22. Liu, S.J. Study on Shale Oil Accumulation Conditions and Sweet Spot Evaluation in the Songliao Basin. Master's Thesis, Xi'an Shiyou University, Xi'an, China, 2022. (In Chinese)
23. Zhang, M.; Tang, Y.J.; Xu, X.Y.; Bai, J.; Li, H.B. Heterogeneity evaluation of mud shale in the first member of the Qingshankou Formation, Changling Sag, Songliao Basin: A case study of Well Jiyeyou 1. *Geol. Resour.* **2021**, *30*, 265–272. (In Chinese)
24. *GB/T 19145-2022*; Determination for Total Organic Carbon in Sedimentary Rock. Standards Press of China: Beijing, China, 2022.
25. Poulton, S.W.; Canfield, D.E. Development of a sequential extraction procedure for iron: Implications for iron partitioning in continentally derived particulates. *Chem. Geol.* **2005**, *214*, 209–221. [CrossRef]
26. Canfield, D.E.; Raiswell, R.; Westrich, J.T.; Reaves, C.M.; Berner, R.A. The use of chromium reduction in the analysis of reduced inorganic sulfur in sediments and shales. *Chem. Geol.* **1986**, *54*, 149–155. [CrossRef]
27. *GB/T 14506.28-2010*; Methods for Chemical Analysis of Silicate Rocks—Part 28. Standards Press of China: Beijing, China, 2010.
28. Carvalho, L.; Reis, A.T.; Soares, E.; Tavares, C.; Monteiro, R.J. A single digestion procedure for determination of major, trace, and rare earth elements in sediments. *Water Air Soil Pollut.* **2020**, *231*, 541. [CrossRef]
29. *SY/T 5735-2019*; Geochemical Method for Source Rock Evaluation. Standards Press of China: Beijing, China, 2019.
30. Raiswell, R.; Canfield, D.E. Sources of iron for pyrite formation in marine sediments. *Am. J. Sci.* **1998**, *298*, 219–245. [CrossRef]
31. Raiswell, R.; Hardisty, D.S.; Lyons, T.W.; Canfield, D.E.; Owens, J.D.; Planavsky, N.J.; Poulton, S.W.; Reinhard, C.T. The iron paleoredox proxies: A guide to the pitfalls, problems and proper practice. *Am. J. Sci.* **2018**, *318*, 491–526. [CrossRef]
32. Poulton, S.W.; Raiswell, R. The low-temperature geochemical cycle of iron: From continental fluxes to marine sediment deposition. *Am. J. Sci.* **2002**, *302*, 774–805. [CrossRef]
33. Taylor, S.R.; McLennan, S.M. *The Continental Crust: Its Composition and Evolution*; Blackwell Scientific Publications: Oxford, UK, 1985; 312p.
34. Hayashi, K.I.; Fujisawa, H.; Holland, H.D.; Ohmoto, H. Geochemistry of ~1.9 Ga sedimentary rocks from northeastern Labrador, Canada. *Geochim. Cosmochim. Acta* **1997**, *61*, 4115–4137. [CrossRef] [PubMed]
35. Wu, F.Y.; Sun, D.Y.; Li, H.M.; Wang, X.L. The nature of basement beneath the Songliao Basin in NE China: Geochemical and isotopic constraints. *Phys. Chem. Earth Part A Solid Earth Geod.* **2001**, *26*, 793–803. [CrossRef]
36. Cullers, R.L. The controls on the major and trace element variation of shales, siltstones, and sandstones of Pennsylvanian-Permian age from uplifted continental blocks in Colorado to platform sediment in Kansas, USA. *Geochim. Cosmochim. Acta* **1994**, *58*, 4955–4972. [CrossRef]
37. McLennan, S.M.; Hemming, S.; McDaniel, D.K.; Hanson, G.N. Geochemical approaches to sedimentation, provenance, and tectonics. In *Processes Controlling the Composition of Clastic Sediments*; Johnsson, M.J., Basu, A., Eds.; Geological Society of America: Boulder, CO, USA, 1993; Volume 284, pp. 21–40.
38. Meng, Q.T.; Liu, Z.J.; Hu, F.; Sun, P.C.; Liu, R.; Zhou, R.J.; Zhen, Z. Rare earth element geochemistry and its geological significance of Eocene oil shale in the Huadian Basin. *J. Jilin Univ. Earth Sci. Ed.* **2013**, *43*, 390–399. (In Chinese)
39. Nesbitt, H.W.; Young, G.M. Early Proterozoic climates and plate motions inferred from major element chemistry of lutites. *Nature* **1982**, *299*, 715–717. [CrossRef]
40. McLennan, S.M. Weathering and global denudation. *J. Geol.* **1993**, *101*, 295–303. [CrossRef]
41. Fedo, C.M.; Nesbitt, H.W.; Young, G.M. Unraveling the effects of potassium metasomatism in sedimentary rocks and paleosols, with implications for paleoweathering conditions and provenance. *Geology* **1995**, *23*, 921–924. [CrossRef]
42. Brimhall, G.H.; Dietrich, W.E. Constitutive mass balance relations between chemical composition, volume, density, porosity, and strain in metasomatic hydrochemical systems: Results on weathering and pedogenesis. *Geochim. Cosmochim. Acta* **1987**, *51*, 567–587. [CrossRef]
43. Rasmussen, C.; Brantley, S.; Richter, D.B. Strong climate and tectonic control on plagioclase weathering in granitic terrain. *Earth Planet. Sci. Lett.* **2011**, *301*, 521–530. [CrossRef]
44. Chamberlain, C.P.; Wan, X.; Graham, S.A.; Carroll, A.R.; Doebbert, A.C.; Sageman, B.B.; Blisniuk, P.; Kent-Corson, M.L.; Wang, Z.; Chengshan, W. Stable isotopic evidence for climate and basin evolution of the Late Cretaceous Songliao basin, China. *Palaeogeogr. Palaeoclimatol. Palaeoecol.* **2013**, *385*, 106–124. [CrossRef]
45. Wang, C.; Feng, Z.; Zhang, L.; Huang, Y.; Cao, K.; Wang, P.; Zhao, B. Cretaceous paleogeography and paleoclimate and the setting of SKI borehole sites in Songliao Basin, northeast China. *Palaeogeogr. Palaeoclimatol. Palaeoecol.* **2013**, *385*, 17–30. [CrossRef]

46. Liu, Y.; Wang, X.; Wu, M.; Su, J.; Yuan, C.; Qi, X.; Zhang, S. A 500-kyr pluvial interval triggered lacustrine carbon burial in Late Cretaceous East Asia. *Geophys. Res. Lett.* **2026**, *53*, e2025GL119676. [CrossRef]
47. Crusius, J.; Calvert, S.; Pedersen, T.; Sage, D. Rhenium and molybdenum enrichments in sediments as indicators of oxic, suboxic and sulfidic conditions of deposition. *Earth Planet. Sci. Lett.* **1996**, *145*, 65–78. [CrossRef]
48. Dean, W.E.; Gardner, J.V.; Piper, D.Z. Inorganic geochemical indicators of glacial-interglacial changes in productivity and anoxia on the California continental margin. *Geochim. Cosmochim. Acta* **1997**, *61*, 4507–4518. [CrossRef]
49. Harris, N.B.; Freeman, K.H.; Pancost, R.D.; White, T.S.; Mitchell, G.D. The character and origin of lacustrine source rocks in the Lower Cretaceous synrift section, Congo Basin, West Africa. *AAPG Bull.* **2004**, *88*, 1163–1184. [CrossRef]
50. Tribovillard, N.; Algeo, T.J.; Lyons, T.; Riboulleau, A. Trace metals as paleoredox and paleoproductivity proxies: An update. *Chem. Geol.* **2006**, *232*, 12–32. [CrossRef]
51. Yin, J.; Wang, Q.; Hao, F.; Guo, L.X.; Zou, H.Y. Palaeoenvironmental reconstruction of lacustrine source rocks in the lower first member of the Shahejie Formation in the Raoyang Sag and the Baxian Sag, Bohai Bay Basin, eastern China. *Palaeogeogr. Palaeoclimatol. Palaeoecol.* **2018**, *495*, 87–104. [CrossRef]
52. Algeo, T.J.; Maynard, J.B. Trace-element behavior and redox facies in core shales of Upper Pennsylvanian Kansas-type cyclothems. *Chem. Geol.* **2004**, *206*, 289–318. [CrossRef]
53. Algeo, T.J.; Liu, J. A re-assessment of elemental proxies for paleoredox analysis. *Chem. Geol.* **2020**, *540*, 119549. [CrossRef]
54. Poulton, S.W.; Canfield, D.E. Ferruginous conditions: A dominant feature of the ocean through Earth's history. *Elements* **2011**, *7*, 107–112. [CrossRef]
55. Anderson, T.F.; Raiswell, R. Sources and mechanisms for the enrichment of highly reactive iron in euxinic Black Sea sediments. *Am. J. Sci.* **2004**, *304*, 203–233. [CrossRef]
56. Zhang, W.; Jin, Z.; Liu, Q.; Shan, X.; Li, P.; Liang, X. The C–S–Fe system evolution reveals organic matter preservation in lacustrine shales of Yanchang Formation, Ordos Basin, China. *Mar. Pet. Geol.* **2022**, *142*, 105750. [CrossRef]
57. Johnson, J.E.; MacLeod, K.G.; Quinn, J.; Fullagar, P.D. Nascent oxygenic phototrophy in the Late Archean: A possible trigger for global oxidation. *Earth Planet. Sci. Lett.* **2008**, *265*, 209–220.
58. Jia, J.L.; Bechtel, A.; Liu, Z.J.; Strobl, S.A.I.; Sun, P.C.; Sachsenhofer, R.F. Oil shale formation in the Upper Cretaceous Nenjiang Formation of the Songliao Basin (NE China): Implications from organic and inorganic geochemical analyses. *Int. J. Coal Geol.* **2013**, *113*, 11–26. [CrossRef]
59. Wang, Y.; Mao, C.; Duan, X. Coupling of paleosedimentary environment and lithofacies: Implications for shale oil enrichment in the Lianggaoshan Formation, northeastern Sichuan Basin, China. *ACS Omega* **2024**, *9*, 28237–28252. [CrossRef] [PubMed]
60. Frederickson, A.F.; Reynolds, R.C., Jr. Geochemical method for determining paleosalinity. In *Clays and Clay Minerals*; Pergamon Press: Oxford, UK, 1960; Volume 8, pp. 203–213.
61. Lerman, A. Boron in clays and estimation of paleosalinities. *Sedimentology* **1966**, *6*, 267–286. [CrossRef]
62. Wei, W.; Algeo, T.J. Elemental proxies for paleosalinity analysis of ancient shales and mudrocks. *Geochim. Cosmochim. Acta* **2020**, *287*, 341–366. [CrossRef]
63. Wang, Y.; Guo, W.; Zhang, G. Application of some geochemical indicators in determining the sedimentary environment of the Funing Group (Paleogene), Jinhu Depression. *J. Tongji Univ. (Nat. Sci.)* **1979**, *7*, 54–63. (In Chinese)
64. Dypvik, H.; Harris, N.B. Geochemical facies analysis of fine-grained siliciclastics using Th/U, Zr/Rb and (Zr + Rb)/Sr ratios. *Chem. Geol.* **2001**, *181*, 131–146. [CrossRef]
65. Young, G.M.; Nesbitt, H.W. Processes controlling the distribution of Ti and Al in weathering profiles, siliciclastic sediments and sedimentary rocks. *J. Sediment. Res.* **1998**, *68*, 448–455. [CrossRef]
66. Wijesinghe, P.; Littke, R.; Burnaz, L.; Blumenberg, M.; Erbacher, J.; Mann, T.; Amann, F.; Bauersachs, T. Black shale deposition during the Early Jurassic: Geochemistry of Pliensbachian and Toarcian sedimentary rocks of the Hunzen Well, Hils Syncline, Northwest German Basin. *Depos. Rec.* **2025**, *11*, 1451–1478. [CrossRef]
67. Deer, W.A.; Howie, R.A.; Zussman, J. *An Introduction to the Rock-Forming Minerals*; Mineralogical Society of Great Britain and Ireland: London, UK, 2013.
68. He, W.; Zhao, Y.; Zhong, J.; Sun, N. Characteristics and significance of micron pores and micron fractures in shale oil reservoirs of Cretaceous Qingshankou Formation in Gulong Sag, Songliao Basin. *Lithol. Reserv.* **2024**, *36*, 1–18. (In Chinese)
69. Ingall, E.D.; Bustin, R.M.; Van Cappellen, P. Influence of water column anoxia on the burial and preservation of carbon and phosphorus in marine shales. *Geochim. Cosmochim. Acta* **1993**, *57*, 303–316. [CrossRef]
70. Vink, S.; Chambers, R.M.; Smith, S.V. Distribution of phosphorus in sediments from Tomales Bay, California. *Mar. Geol.* **1997**, *139*, 157–179. [CrossRef]
71. Dymond, J.; Suess, E.; Lyle, M. Barium in deep-sea sediment: A geochemical proxy for paleoproductivity. *Paleoceanography* **1992**, *7*, 163–181. [CrossRef]

72. Latimer, J.C.; Filippelli, G.M. Eocene to Miocene terrigenous inputs and export production: Geochemical evidence from ODP Leg 177, Site 1090. *Palaeogeogr. Palaeoclimatol. Palaeoecol.* **2002**, *182*, 151–164. [CrossRef]
73. Brockamp, O. Delamination of smectite in river-borne suspensions at the fluvial/marine interface—An experimental study. *Estuar. Coast. Shelf Sci.* **2011**, *91*, 33–41. [CrossRef]

Disclaimer/Publisher's Note: The statements, opinions and data contained in all publications are solely those of the individual author(s) and contributor(s) and not of MDPI and/or the editor(s). MDPI and/or the editor(s) disclaim responsibility for any injury to people or property resulting from any ideas, methods, instructions or products referred to in the content.